European Journal of Mechanics A/Solids 28 (2009) 402–416

Contents lists available at ScienceDirect

European Journal of Mechanics A/Solids

www.elsevier.com/locate/ejmsol

A finite-strain model for anisotropic viscoplastic porous media: II – Applications

K. Danas [a,b], P. Ponte Castañeda [a,b,*]

[a] *Department of Mechanical Engineering and Applied Mechanics, University of Pennsylvania, Philadelphia, PA 19104-6315, USA*
[b] *Laboratoire de Mécanique des Solides, C.N.R.S. UMR7649, Département de Mécanique, École Polytechnique, 91128 Palaiseau Cedex, France*

ARTICLE INFO

Article history:
Received 17 July 2008
Accepted 7 November 2008
Available online 19 November 2008

Keywords:
Porous media
Homogenization
Viscoplasticity
Constitutive model
Microstructure evolution

ABSTRACT

In Part I of this work, we have proposed a new model based on the "second-order" nonlinear homogenization method for determining the effective response and microstructure evolution in viscoplastic porous media with aligned ellipsoidal voids subjected to general loading conditions. In this second part, the new model is used to analyze the instantaneous effective behavior and microstructure evolution in porous media for several representative loading conditions and microstructural configurations. First, we study the effect of the shape and orientation of the voids on the overall instantaneous response of a porous medium that is subjected to principal loading conditions. Secondly, we study the problem of microstructure evolution under axisymmetric and simple shear loading conditions for initially spherical voids in an attempt to validate the present model by comparison with existing numerical and approximate results in the literature. Finally, we study the possible development of macroscopic instabilities for the special case of ideally-plastic solids subjected to plane-strain loading conditions. The results, reported in this paper, suggest that the present model improves dramatically on the earlier "variational" estimates, in particular, because it generates much more accurate results for high triaxiality loading conditions.

1. Introduction

In the first part of this paper (Danas and Ponte Castañeda, 2009), henceforth referred to as Part I, we have proposed an approximate model for the determination of the instantaneous effective behavior and microstructure evolution in *anisotropic* viscoplastic porous materials subjected to general loading conditions. The new model is based on the nonlinear "second-order" homogenization method of Ponte Castañeda (2002a), where a certain "reference" stress tensor is chosen to recover exactly the behavior of a "composite-sphere assemblage" in the limit of hydrostatic loadings, therefore coinciding with the hydrostatic limit of the Gurson's criterion in the special case of ideal plasticity. The new model has also been extended, in an approximate manner, to take into account general "ellipsoidal" microstructures (i.e., orthotropic symmetry of the material) and three-dimensional loading conditions. The internal variables characterizing the microstructure have been denoted by the set

$$s_\alpha = \left\{ f, w_1, w_2, \mathbf{n}^{(1)}, \mathbf{n}^{(2)}, \mathbf{n}^{(3)} = \mathbf{n}^{(1)} \times \mathbf{n}^{(2)} \right\}, \tag{1}$$

where f is the porosity, $w_1 = a_3/a_1$ and $w_2 = a_3/a_2$ are the two aspect ratios defining the shape of the ellipsoidal void (with a_1, a_2 and a_3 denoting the principal semi-axes of the ellipsoidal voids), while the vectors $\mathbf{n}^{(i)}$ (with $i = 1, 2, 3$) denote the orientation of the principal axes of the voids.

In the present paper, the new model is applied to various loading conditions and is compared to other models and available numerical results. More specifically, this study is divided in two main parts. The first part involves the study of the instantaneous effective response of porous materials for a given microstructural and loading configuration, and is detailed in Section 2. The porous media under study consist of ellipsoidal voids, whose principal axes can be aligned or misaligned with the principal loading directions. The new model is compared with available estimates by the "variational" method of Ponte Castañeda (1991), Ponte Castañeda and Zaidman (1994), Kailasam and Ponte Castañeda (1998), Aravas and Ponte Castañeda (2004), which is also valid for general ellipsoidal microstructures and loading conditions, and the recently proposed Flandi and Leblond (2005a, 2005b) model, which is valid only for spheroidal voids, but has been heuristically extended to predict the instantaneous response (but not the evolution of microstructure) for arbitrary stress loadings. In addition, comparisons of the above models with numerical results for the special cases of spherical and cylindrical voids corresponding to isotropic and transversely isotropic microstructures, respectively, have already been given in Danas et al. (2008b) and Danas et al. (2008a, 2008c) and will not be repeated here. In particular, the results for the isotropic case

---

[*] Corresponding author at: Department of Mechanical Engineering and Applied Mechanics, University of Pennsylvania, Philadelphia, PA 19104-6315, USA. Tel.: +1 215 898 5046; fax: +1 215 573 6334.

E-mail addresses: kdanas@seas.upenn.edu (K. Danas), ponte@seas.upenn.edu (P. Ponte Castañeda).

0997-7538/$ – see front matter © 2008 Elsevier Masson SAS. All rights reserved.
doi:10.1016/j.euromechsol.2008.11.003

show an interesting dependence on the third invariant (i.e., on the Lode angle).

In turn, the second part of this paper (Sections 3–5) is devoted to the study of microstructure evolution in porous media with initially spherical voids. In this part, we compare the estimates of this new model with the "variational" estimates (Ponte Castañeda and Zaidman, 1994; Kailasam and Ponte Castañeda, 1998; Aravas and Ponte Castañeda, 2004), the Flandi and Leblond (2005b) model and unit-cell finite element calculations for axisymmetric loading conditions and initially spherical voids. In addition, we consider simple shear loading in Section 4 leading to rotation of the voids and therefore of the anisotropy axes. Finally, we apply the present model to analyze the possible development of shear localization in ideally plastic solids under plane-strain loading conditions. It is emphasized that the "second-order" and the "variational" methods are the only available methods in the literature that are capable of providing estimates for the effective behavior and microstructure evolution under general (e.g., non-aligned) loading conditions leading to general ellipsoidal microstructures as the deformation progresses. Additional examples have been considered in Danas (2008).

2. Instantaneous effective behavior

The main objective of this section is to study the *instantaneous* effective behavior of anisotropic porous materials in the simplest possible way. In general, the behavior of such materials depends on all microstructural variables s_a, as well as on all six components of the macroscopic stress tensor $\overline{\boldsymbol{\sigma}}$. However, for simplicity, we will consider fully triaxial loading (i.e., the principal loading directions coinciding with the laboratory frame of reference), while letting the microstructure be aligned or misaligned with these principal directions.

In the presentation of the results, use of the gauge surface will be made. It is useful to recall that the gauge surface generalizes the notion of the yield surface in the context of viscoplastic materials and has been detailed in Section 2.3 of Part I (not repeated here). For completeness and conciseness, it is useful to note that the gauge function is defined in terms of the gauge factor Γ_n via

$$\widetilde{\Phi}_n(\boldsymbol{\Sigma}; s_\alpha) = \Gamma_n(\boldsymbol{\Sigma}; s_\alpha) - 1, \tag{2}$$

such that the condition $\widetilde{\Phi}_n = 0$ defines the corresponding gauge surface in the space of the normalized second-order stress tensors $\boldsymbol{\Sigma} = \overline{\boldsymbol{\sigma}}/\Gamma_n(\overline{\boldsymbol{\sigma}})$ (see relation (9) of Part I). In the following, we present certain cross-sections of this gauge surface for several microstructural and loading configurations to be discussed below. Note further that the subscript n ($m = 1/n$ is the strain-rate sensitivity parameter) refers to the nonlinear exponent associated with the matrix phase (see relation (1) of Part I). The two limiting values $n = 1$ (or $m = 1$) and $n \to \infty$ (or $m = 0$) correspond to linear and ideally-plastic behaviors, respectively.

Loading configuration. Let the principal directions of the macroscopic stress tensor $\overline{\boldsymbol{\sigma}}$, or, equivalently, $\boldsymbol{\Sigma}$, be aligned with a fixed Cartesian laboratory frame of reference defined by the three unit vectors $\mathbf{e}^{(i)}$ (with $i = 1, 2, 3$). Then, the normalized macroscopic stress tensor $\overline{\boldsymbol{\Sigma}}$ can be represented in terms of its three principal values $\overline{\Sigma}_1$, $\overline{\Sigma}_2$, $\overline{\Sigma}_3$, or, equivalently, in terms of the principal values of the deviatoric stress tensor, i.e., $\overline{\Sigma}'_1$, $\overline{\Sigma}'_2$, $\overline{\Sigma}'_3$ (with $\overline{\Sigma}'_1 + \overline{\Sigma}'_2 + \overline{\Sigma}'_3 = 0$) and the mean stress $\overline{\Sigma}_m$, via

$$\begin{aligned}\overline{\boldsymbol{\Sigma}} &= \overline{\Sigma}_m \boldsymbol{\delta} + \overline{\Sigma}_{eq} \overline{\mathbf{S}} \\ &= \overline{\Sigma}_m \boldsymbol{\delta} + \overline{\Sigma}'_1 \mathbf{e}^{(1)} \otimes \mathbf{e}^{(1)} + \overline{\Sigma}'_2 \mathbf{e}^{(2)} \otimes \mathbf{e}^{(2)} + \overline{\Sigma}'_3 \mathbf{e}^{(3)} \otimes \mathbf{e}^{(3)}.\end{aligned} \tag{3}$$

The stress quantities $\overline{\Sigma}_m = \overline{\Sigma}_1 + \overline{\Sigma}_2 + \overline{\Sigma}_3$ and $\overline{\Sigma}_{eq} = \sqrt{3\overline{\boldsymbol{\Sigma}}' \cdot \overline{\boldsymbol{\Sigma}}'/2}$ are the normalized macroscopic mean and von Mises equivalent stress measures, respectively, while $\boldsymbol{\delta}$ is the identity, $\overline{\mathbf{S}} = \overline{\boldsymbol{\sigma}}'/\overline{\sigma}_{eq} = \overline{\boldsymbol{\Sigma}}'/\overline{\Sigma}_{eq}$ is a normalized stress tensor and $\overline{\boldsymbol{\Sigma}}'$ is the stress deviator.

Making use of the previous notation and following the work of (Danas et al., 2008b), we define the stress quantities

$$X_\Sigma = \frac{\overline{\Sigma}_m}{\overline{\Sigma}_{eq}}, \qquad \cos(3\theta) = \frac{27}{2}\det(\overline{\mathbf{S}}). \tag{4}$$

The first is the stress triaxiality, and the second is the Lode angle (Kachanov, 1971) in stress space, which is related to the determinant of the macroscopic deviatoric stress tensor $\overline{\boldsymbol{\Sigma}}'$ and lies between $0 \leqslant \theta < 2\pi$. The values $\theta = N\pi/3$ and $\theta = (2N+1)\pi/6$, with N (< 6) being a positive integer, correspond to axisymmetric and simple shear loading conditions, respectively. It is important to emphasize that if the porous medium is anisotropic (which is the case in this work), the effective behavior of the material will be different for the various values of the integer N. Relation $(4)_2$ may then be inverted so that, relative to its principal axes, $\overline{\mathbf{S}}$ is represented in terms of the Lode angle θ through

$$\overline{\mathbf{S}} = \frac{2}{3}\operatorname{diag}\left\{-\cos\left(\theta + \frac{\pi}{3}\right), -\cos\left(\theta - \frac{\pi}{3}\right), \cos(\theta)\right\}. \tag{5}$$

In view of definition (2), it is convenient to define two cross-sections of the gauge surface of the porous material. One cross-section may be defined by considering $\theta = const$. This cross-section lies on a plane which is described by the Cartesian coordinates $\overline{\Sigma}_{eq}$ and $\overline{\Sigma}_m$, and is also known as the *meridional plane*.

An alternative cross-section of the gauge surface may be considered on a plane defined by a constant hydrostatic pressure, i.e. $\overline{\Sigma}_m = const$. This projection is equivalent to the standard deviatoric Π-plane (or else octahedral plane) in the theory of plasticity. The polar coordinates on this plane are $r = \sqrt{2/3}\,\overline{\Sigma}_{eq}$ and the Lode angle θ, respectively. For convenience, in-plane Cartesian coordinates may also be defined (Lubliner, 1990) by using definitions (3) and (5), such that

$$\begin{aligned} x &= \frac{2\overline{\Sigma}_3 - \overline{\Sigma}_1 - \overline{\Sigma}_2}{\sqrt{6}} = \sqrt{\frac{3}{2}}\,\overline{\Sigma}'_3 = \sqrt{\frac{2}{3}}\,\overline{\Sigma}_{eq}\cos(\theta), \\ y &= \frac{\overline{\Sigma}_1 - \overline{\Sigma}_2}{\sqrt{2}} = \frac{\overline{\Sigma}'_1 - \overline{\Sigma}'_2}{\sqrt{2}} = \sqrt{\frac{2}{3}}\,\overline{\Sigma}_{eq}\sin(\theta). \end{aligned} \tag{6}$$

Microstructural configuration. The microstructural configurations to be studied in this work are shown schematically in Fig. 1. In case (a), we consider prolate spheroidal voids with aspect ratios $w_1 = w_2 = 5$, whose major (symmetry) axis is aligned with the $\mathbf{n}^{(3)}$-direction. The second configuration (b) involves oblate spheroidal voids with aspect ratios $w_1 = w_2 = 0.2$, whose minor (symmetry) axis is aligned with the $\mathbf{n}^{(3)}$-direction. The third case (c) concerns ellipsoidal voids with two different aspect ratios $w_1 = a_3/a_1 = 5$ and $w_2 = a_3/a_2 = 0.2$, whose major axis is aligned with the $\mathbf{n}^{(2)}$-direction and the minor axis with $\mathbf{n}^{(1)}$-direction. This last case has been introduced to emphasize the importance of having a model that is capable of handling ellipsoidal microstructures that are more general than the spheroidal microstructures (i.e., voids having one circular cross-section).

The principal directions of the voids, i.e., $\mathbf{n}^{(i)}$, need not be aligned with the principal loading directions $\mathbf{e}^{(i)}$. In this case, the overall behavior of the composite is expected to exhibit general anisotropy and such cases are considered in the following. In order to describe the orientation of the principal axes of the voids $\mathbf{n}^{(i)}$ with respect to the fixed loading directions $\mathbf{e}^{(i)}$, we employ the standard notation that has been widely used to describe the slip direction of single crystals (Miller indices in crystallography). In this connection, the notation $\mathbf{n}^{(1)} = [0\,1\,\bar{1}]$, implies that $\mathbf{n}^{(1)} = 0\mathbf{e}^{(1)} + 1/\sqrt{2}\mathbf{e}^{(2)} - 1/\sqrt{2}\mathbf{e}^{(3)}$.

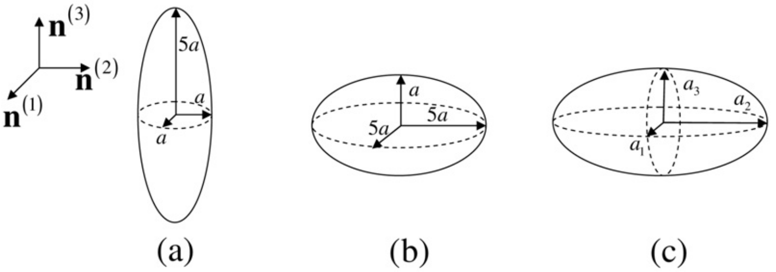

Fig. 1. Void shapes in the frame of reference defined by the vectors $\mathbf{n}^{(i)}$ which correspond to the orientation of the principal axes of the voids. Three configurations are considered: (a) prolate voids with aspect ratios $w_1 = w_2 = 5$, (b) oblate voids with aspect ratios $w_1 = w_2 = 0.2$ and (c) ellipsoidal voids with aspect ratios $w_1 = 5$ and $w_2 = 0.2$.

2.1. Meridional planes for aligned microstructures

This subsection deals with the determination of the instantaneous effective behavior of porous materials consisting of voids with prolate, oblate or ellipsoidal shapes, as shown in Fig. 1, whose principal axes $\mathbf{n}^{(i)}$ $(i = 1, 2, 3)$ coincide with the principal loading directions and therefore with $\mathbf{e}^{(i)}$ $(i = 1, 2, 3)$, such that $\mathbf{n}^{(i)} = \mathbf{e}^{(i)}$. Consequently, the instantaneous response of the porous medium is, in general, orthotropic, while the axes of orthotropy coincide with the principal loading directions $\mathbf{e}^{(i)}$.

Then, let these materials be subjected to two types of loading conditions, which are expressed according to (3) and (5) by

$$\overline{\boldsymbol{\Sigma}} = \overline{\Sigma}_m \boldsymbol{\delta} + \frac{T}{3}\left(-\mathbf{e}^{(1)} \otimes \mathbf{e}^{(1)} - \mathbf{e}^{(2)} \otimes \mathbf{e}^{(2)} + 2\mathbf{e}^{(3)} \otimes \mathbf{e}^{(3)}\right), \quad (AXS) \tag{7}$$

and

$$\overline{\boldsymbol{\Sigma}} = \begin{cases} \overline{\Sigma}_m \boldsymbol{\delta} + T/\sqrt{3}(\mathbf{e}^{(1)} \otimes \mathbf{e}^{(1)} - \mathbf{e}^{(2)} \otimes \mathbf{e}^{(2)}), & (PS12) \\ \overline{\Sigma}_m \boldsymbol{\delta} + T/\sqrt{3}(\mathbf{e}^{(1)} \otimes \mathbf{e}^{(1)} - \mathbf{e}^{(3)} \otimes \mathbf{e}^{(3)}), & (PS13) \\ \overline{\Sigma}_m \boldsymbol{\delta} + T/\sqrt{3}(\mathbf{e}^{(2)} \otimes \mathbf{e}^{(2)} - \mathbf{e}^{(3)} \otimes \mathbf{e}^{(3)}), & (PS23). \end{cases} \tag{8}$$

In the above expressions, $\overline{\Sigma}_m$ denotes the mean stress, while $T = \pm\overline{\Sigma}_{eq}$, such that the corresponding stress triaxiality reduces to $X_\Sigma = \overline{\Sigma}_m/|T|$. The first of the two stress states, given by (7), is an axisymmetric loading, denoted as AXS, with the maximum (absolute) stress component in the 3-direction. The second set of stress states given by (8) is a combination of in-plane 1–2, 1–3 and 2–3 shear loadings with superimposed pressure $\overline{\Sigma}_m$, denoted as $PS12$, $PS13$ and $PS23$, respectively.

Note further that when an axisymmetric loading of the form (7) is applied in the case of prolate or oblate voids (see Fig. 1a, b), whose symmetry axis is aligned with the maximum absolute principal stress, the composite exhibits a transversely isotropic response about the 3-axis, provided that the behavior of the matrix phase is isotropic. Those two microstructural states, i.e., prolate and oblate voids together with the loading condition (7) have also been studied by Flandi and Leblond (2005a, 2005b) (*FL*) in their model and their estimates will be included in this study for comparison with the corresponding "second-order" (*SOM*) predictions. For completeness, we will also include corresponding numerical (*NUM*) results obtained by Flandi and Leblond (2005b) for a confocal spheroidal volume element subjected to the axisymmetric loading conditions (7). These results were obtained via numerical minimization of the macroscopic viscous potential over a family of trial velocity fields especially adapted to the spheroidal geometry according to the work of Lee and Mear (1992).

On the other hand, when the second set of loading conditions (8) is considered, the porous medium exhibits orthotropic behavior. For this last case, Flandi and Leblond have proposed an extension of their model to arbitrary stress states. However, such results will only be shown in Section 2.2, for the effective behavior of the porous medium on the Π-plane. Finally, when the void is ellipsoidal in shape (see Fig. 1c) with two different aspect ratios, the porous material exhibits orthotropic response and hence, only the *SOM* model will be shown for this case.

Due to the fact that the porous material is in general orthotropic, different loading conditions with the same stress triaxiality X_Σ result in different effective behaviors. In this connection, there are two questions that need to be answered. The first one is related to the effect of the void shape on the effective behavior of the porous medium for a given loading. The second question is linked to the effect of the loading on the effective behavior of the porous material for a given void shape. An attempt to provide answers to these two questions will be made in the following.

Fig. 2 shows gauge curves, as predicted by the *SOM* and *FL* models, as well as the numerical spheroidal shell *NUM* results, on the meridional plane $\overline{\Sigma}_m$–T, for a porous material consisting of (a) prolate voids with $w_1 = w_2 = 5$ and (b) oblate voids with $w_1 = w_2 = 0.2$ (see Fig. 1a,b) subjected to the axisymmetric loading conditions defined by (7), while the nonlinear exponent of the matrix phase is $n = 5$ (or $m = 0.2$). For prolate voids, in Fig. 2a, the *SOM* and the *FL* estimates are found to be in good agreement with the *NUM* results for all the porosities $f = 0.1, 1, 10\%$ considered. On the other hand, for oblate voids in Fig. 2b, the *SOM* and the *FL* models give somewhat different estimates, especially near the purely hydrostatic loading (i.e., $T \to 0$), where the *SOM* is found to be more conservative (i.e., softer) than the corresponding *FL* estimate, when compared with the *NUM* results. This difference may be partially attributed to the approximation introduced in the context of the *SOM* for the computation of the hydrostatic point, in Section 2.4 in Part I of this work. On the other hand, it should be emphasized that the *NUM* results are associated with a confocal spheroidal shell, where the shapes of the inner and outer surfaces can be quite different at the larger porosities. Because of this, the comparison of the *NUM* results with the *SOM* predictions becomes inappropriate at large porosities (recall that the shape of the voids and the distribution has been assumed to be the same in the *SOM*, for simplicity).

Fig. 3 shows corresponding *SOM* gauge curves for spheroidal and ellipsoidal voids with aspect ratios $w_1 = w_2 = 5$ (prolate), $w_1 = w_2 = 0.2$ (oblate) and $w_1 = 5$, $w_2 = 0.2$ (general ellipsoid) for a nonlinear exponent $n = 5$ (or $m = 0.2$) and porosity $f = 5\%$. In part (a) of this figure, which corresponds to axisymmetric loading (*cf.* (7) denoted as AXS), the effective behavior of the porous material is found to be substantially different for all three microstructures considered here. The porous medium with ellipsoidal voids ($w_1 = 5$, $w_2 = 0.2$) is softer than the one with oblate voids ($w_1 = w_2 = 0.2$) for stress states lying in the second ($T > 0$ and $\overline{\Sigma}_m < 0$) and the fourth ($T < 0$ and $\overline{\Sigma}_m > 0$) quadrant, while it is significantly softer than the corresponding medium with prolate voids ($w_1 = w_2 = 5$) for all stress states shown in this figure. This implies that the effective gauge curves associated with ellipsoidal voids cannot be approximated by corresponding curves for spheroidal voids, as intuitively expected.

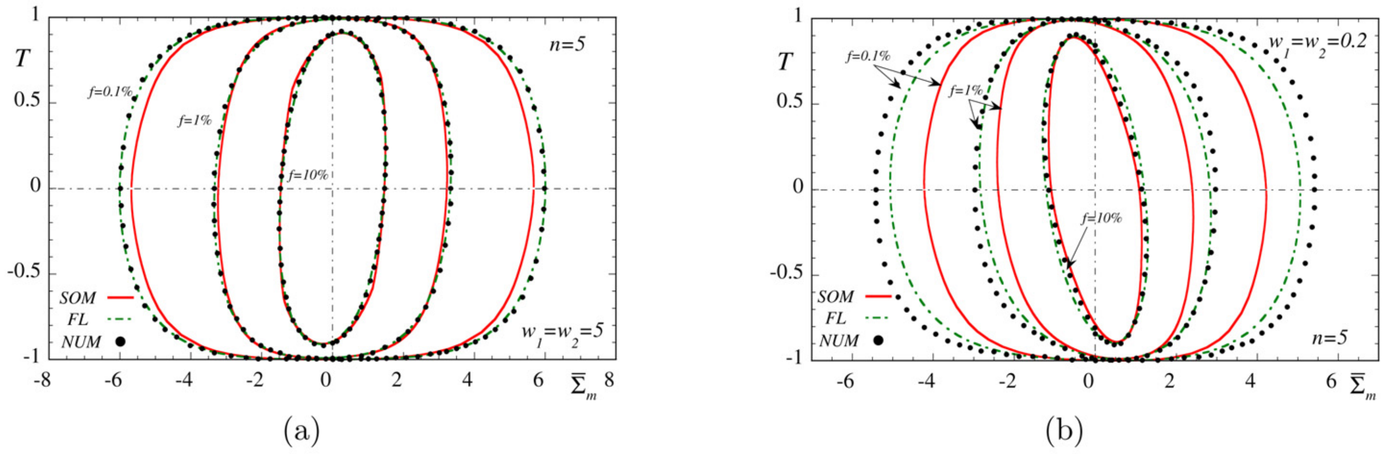

Fig. 2. *SOM*, Flandi and Leblond (2005a, 2005b) (*FL*) and numerical spheroidal shell (*NUM*) gauge surfaces on the $\overline{\Sigma}_m$–T plane for spheroidal voids ($w_1 = w_2$) that are subjected to axisymmetric loading conditions (*cf.* (7)) aligned with the pore symmetry axis. The matrix phase is described by an exponent $n = 5$, while three values of porosity, $f = 0.1, 1, 10\%$ are used. The plots correspond to (a) $w_1 = w_2 = 5$ (prolate voids), and (b) $w_1 = w_2 = 0.2$ (oblate voids).

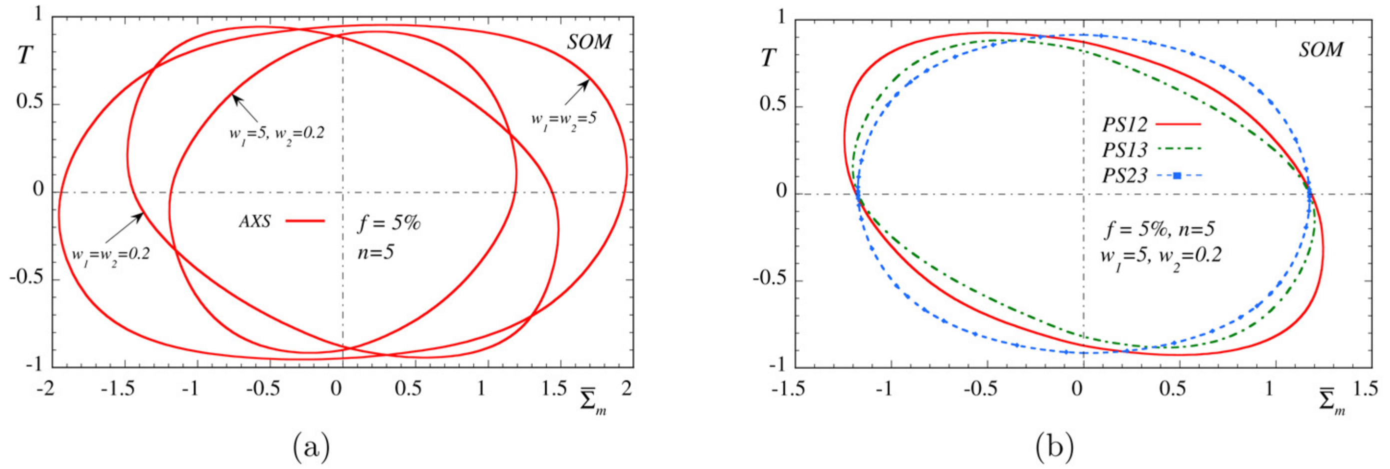

Fig. 3. *SOM* gauge surfaces on the $\overline{\Sigma}_m$–T plane for porous media with (a) prolate ($w_1 = w_2 = 5$), oblate ($w_1 = w_2 = 0.2$) and ellipsoidal ($w_1 = 5$, $w_2 = 0.2$) voids subjected to axisymmetric (*cf.* (7)) loadings and (b) for ellipsoidal ($w_1 = 5$, $w_2 = 0.2$) voids subjected to in-plane shear with superimposed pressure (*cf.* (8)) loading conditions. The matrix phase is described by an exponent $n = 5$, while the porosity is $f = 5\%$.

In Fig. 3b, we present gauge curves only for ellipsoidal voids with $w_1 = 5$ and $w_2 = 0.2$ subjected to in-plane shear with superimposed pressure loadings (*cf.* (8)). Because of the orthotropic symmetry of the material, the plane of shear, i.e., 1–2 plane ($PS12$) or 1–3 plane ($PS13$) or 2–3 plane ($PS23$) has significant effects on the effective response of the porous medium. While the $PS23$ curve appears to be slightly asymmetric about the T-axis, the $PS12$ curve exhibits a significant hardening in the second ($T > 0$ and $\overline{\Sigma}_m < 0$) and fourth ($T < 0$ and $\overline{\Sigma}_m > 0$) quadrant. In addition, it should be noted that the corresponding curve for ellipsoidal voids in part (a) of this figure for *AXS* loading is significantly different than the ones in part (b) for in-plane shear loadings. This implies that the type of loading has significant effects on the macroscopic behavior of the porous medium. On the other hand, we emphasize that all the gauge curves associated with a given microstructural configuration—for instance ellipsoidal voids with $w_1 = 5$ and $w_2 = 0.2$—coincide in the purely hydrostatic limit ($T = 0$), as they should. Nonetheless, the slope of these curves, which is directly related to the direction of the flow, can be significantly different for the various loading conditions.

2.2. Deviatoric planes for anisotropic porous media

In this subsection, we present cross-sections of the gauge surfaces on the Π-plane (deviatoric or octahedral plane). As already pointed out in the beginning of this section, we assume that the principal directions of the macroscopic stress tensor coincide with the Cartesian frame of reference defined by the three orthonormal vectors $\mathbf{e}^{(i)}$ with $i = 1, 2, 3$. The cross-sections of the gauge surface on the Π-plane are defined by imposing a constant pressure $\overline{\Sigma}_m = const$ and prescribing the in-plane Cartesian coordinates (6). For the results shown below, we choose a constant pressure $\overline{\Sigma}_m = 0.9\overline{\Sigma}^H_m$, with $\overline{\Sigma}^H_m = \overline{\Sigma}^H_m|_{som}$ denoting the mean stress delivered by the *SOM* method for purely hydrostatic loading and a given microstructural configuration (see Appendix B of Part I).

The *SOM* results are shown for (i) prolate voids with aspect ratios $w_1 = w_2 = 5$, (ii) oblate voids with aspect ratios $w_1 = w_2 = 0.2$ and (iii) ellipsoidal voids $w_1 = 5$ and $w_2 = 0.2$. In addition, the principal axes of the voids are allowed to be misaligned with respect to the principal loading directions. For convenience, the following figures are labeled according to Table 1, which indicates the orientation of the principal axes of the voids, $\mathbf{n}^{(i)}$, with respect to the fixed unit vectors $\mathbf{e}^{(i)}$. The relevant notation used in Table 1 has already been discussed at the end of Section 2. In the final

Table 1
Orientation of the principal axes of the voids.

Prolate				Oblate				Ellipsoid			
Cases	$\mathbf{n}^{(1)}$	$\mathbf{n}^{(2)}$	$\mathbf{n}^{(3)}$	Cases	$\mathbf{n}^{(1)}$	$\mathbf{n}^{(2)}$	$\mathbf{n}^{(3)}$	Cases	$\mathbf{n}^{(1)}$	$\mathbf{n}^{(2)}$	$\mathbf{n}^{(3)}$
1_p	–	–	[0 0 1]	1_o	–	–	[0 0 1]	1_e	[1 0 0]	[0 1 0]	[0 0 1]
2_p	–	–	[0 1 0]	2_o	–	–	[0 1 0]	2_e	[0 0 1]	[1 0 0]	[0 1 0]
3_p	–	–	[1 0 0]	3_o	–	–	[1 0 0]	3_e	[0 1 0]	[0 0 1]	[1 0 0]
4_p	–	–	[0 1 1]	4_o	–	–	[0 1 1]	4_e	[1 0 0]	[0 1 1]	$[0\,\bar{1}\,1]$
5_p	–	–	[1 1 0]	5_o	–	–	[1 1 0]	5_e	$[0\,0\,\bar{1}]$	[1 1 0]	$[1\,\bar{1}\,0]$
6_p	–	–	[1 0 1]	6_o	–	–	[1 0 1]	6_e	$[0\,\bar{1}\,0]$	[1 0 1]	$[\bar{1}\,0\,1]$
7_p	–	–	[0 3 4]	7_o	–	–	[0 3 4]	–	–	–	–

part of this subsection, we compare the *SOM* estimates with corresponding estimates obtained by the "variational" method (*VAR*) of Ponte Castañeda (1991) and the Flandi and Leblond (2005a) (*FL*) model (see Appendix B of the relevant work), which is valid only for spheroidal voids, i.e., prolate and oblate shapes.

It should be further emphasized that the prolate and oblate voids have a circular cross-section in the plane defined by the unit normal $\mathbf{n}^{(3)}$, which implies that the direction of the symmetry axis (taken here in the $\mathbf{n}^{(3)}$-direction such that $w_1 = w_2$) completely defines the orientation of the voids with respect to the fixed frame of reference. For this reason, in the first two cases of spheroidal voids, Table 1 provides information only about the orientation of the pore symmetry axis $\mathbf{n}^{(3)}$ relative to the base vectors $\mathbf{e}^{(i)}$. By contrast, in the context of ellipsoidal voids ($w_1 \neq w_2$), it is not sufficient to prescribe only the orientation of the major axis of the voids, which is taken to be aligned with $\mathbf{n}^{(2)}$ in this work (with $w_1 = 5$ and $w_2 = 0.2$), but it is also necessary to provide additional information about the orientation of the minor and middle axis, which are aligned with $\mathbf{n}^{(1)}$ and $\mathbf{n}^{(3)}$, respectively. In the figures to follow, the various cases presented in Table 1, are labeled according to the subscript (p) for prolate, (o) for oblate and (e) for ellipsoidal voids.

Prolate voids. Fig. 4 shows *SOM* gauge curves on the Π-plane for a porous material consisting of prolate voids with aspect ratios $w_1 = w_2 = 5$. The continuous (and dashed) symmetry lines on the graph correspond to the three axisymmetric loading conditions aligned with the three axes of the laboratory frame of reference. Fig. 4a shows results for prolate voids whose principal axes are aligned with the principal loading directions. According to Table 1, the 1_p, 2_p and 3_p curves correspond to prolate voids, whose major (symmetry) axis is aligned with the $\mathbf{e}^{(3)}$, $\mathbf{e}^{(2)}$ and $\mathbf{e}^{(1)}$ directions, respectively.

As already expected, the form of the gauge curves is identical for these three cases. Note that the 2_p and 3_p curves can be obtained by $2\pi/3$ and $4\pi/3$ clockwise rotation of the 1_p curve about the origin. In addition, due to the spheroidal symmetry of the microstructure, the 1_p, 2_p and 3_p curves are symmetric about the $\overline{\Sigma}'_3$-, $\overline{\Sigma}'_2$- and $\overline{\Sigma}'_1$-axis, respectively. A second important observation is linked to the fact that when axisymmetric loading conditions are considered transverse to the pore symmetry axis (e.g., look at 1_p curve when it crosses the positive $\overline{\Sigma}'_2$-axis), the effective behavior of the material is significantly softer than in the case of axisymmetric loading along the pore symmetry axis (e.g., look at 1_p curve when it crosses the positive $\overline{\Sigma}'_3$-axis).

Fig. 4b shows gauge curves for porous media containing prolate voids whose principal axes are misaligned with the principal loading directions. According to Table 1, the curves 4_p, 5_p and 6_p correspond to the cases that the major (symmetry) axis of the voids lies in the 2–3, 1–3 and 1–2 planes, respectively. Similar to the curves in part (a) of this figure, the 5_p and 6_p estimates can be obtained by $2\pi/3$ and $4\pi/3$ clockwise rotation of the 4_p curve about the origin. In addition, the 4_p, 5_p and 6_p curves are symmetric about the $\overline{\Sigma}'_1$-, $\overline{\Sigma}'_3$- and $\overline{\Sigma}'_2$-axis, respectively. This is a direct consequence of the specific choice for the orientation of the symmetry axis of the voids relative to the principal loading directions. Note that the effective behavior of a porous medium with prolate voids, whose symmetry axis is not aligned with the principal loading directions, is, in general, *anisotropic* and thus no symmetry of the gauge surface on the Π-plane should be expected. Indeed, Fig. 4c verifies this observation, where we chose to show the 7_p gauge curve corresponding to prolate voids aligned in the direction [034].

Oblate voids. Fig. 5 shows the corresponding *SOM* gauge curves on the Π-plane for a porous material consisting of oblate voids with aspect ratios $w_1 = w_2 = 0.2$. As before, the continuous (and dashed) symmetry lines on the graph correspond to the three axisymmetric loading conditions aligned with the laboratory frame of reference. Fig. 5a shows gauge curves for porous media containing oblate voids whose minor (symmetry) axis is aligned with the principal loading directions. In accord with Table 1, the curves 1_o, 2_o and 3_o correspond to the cases that the symmetry axis of the voids is aligned with the $\mathbf{e}^{(3)}$, $\mathbf{e}^{(2)}$ and $\mathbf{e}^{(1)}$ direction, respectively. Due to the spheroidal symmetry of the microstructure, the corresponding 1_o, 2_o and 3_o curves are symmetric about the $\overline{\Sigma}'_3$-, $\overline{\Sigma}'_2$- and $\overline{\Sigma}'_1$-axis, respectively. Furthermore, the 2_o and 3_o curves can be obtained by $2\pi/3$ and $4\pi/3$ clockwise rotation of the 1_p

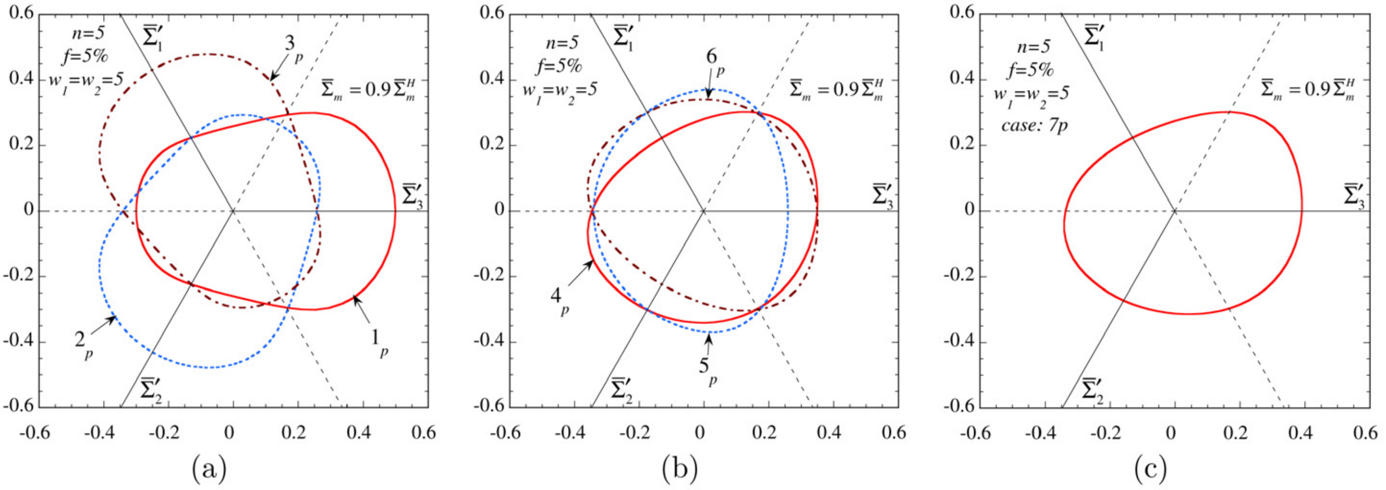

Fig. 4. *SOM* cross-sections of the gauge function on the Π-plane (or octahedral plane) for porous media consisting of prolate voids with aspect ratios $w_1 = w_2 = 5$, porosity $f = 5\%$ and nonlinearity $n = 5$. The relevant graphs correspond to the cases that the pore symmetry axis is (a) aligned (1_p–3_p) and (b)–(c) misaligned (4_p–7_p) with the principal directions of the loading. The cases 1_p–7_p are defined in Table 1.

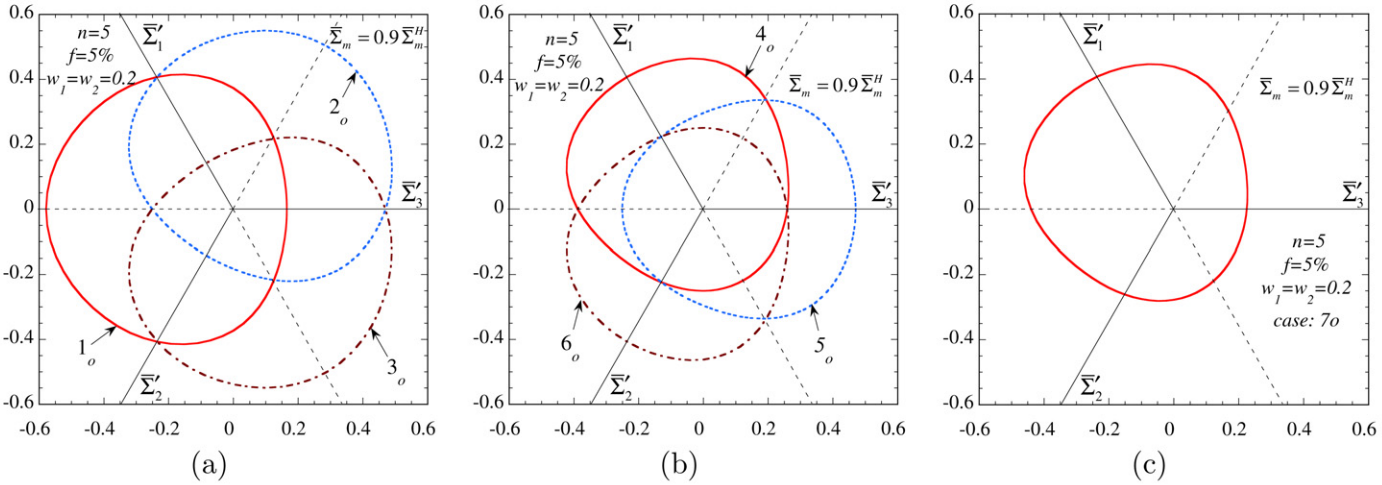

Fig. 5. *SOM* cross-sections of the gauge function on the Π-plane (or octahedral plane) for porous media consisting of oblate voids with aspect ratios $w_1 = w_2 = 0.2$, porosity $f = 5\%$ and nonlinearity $n = 5$. The relevant graphs correspond to the cases that pore symmetry axis is (a) aligned (1_o–3_o) and (b)–(c) misaligned (4_o–7_o) with the principal directions of the loading. The cases 1_o–7_o are defined in Table 1.

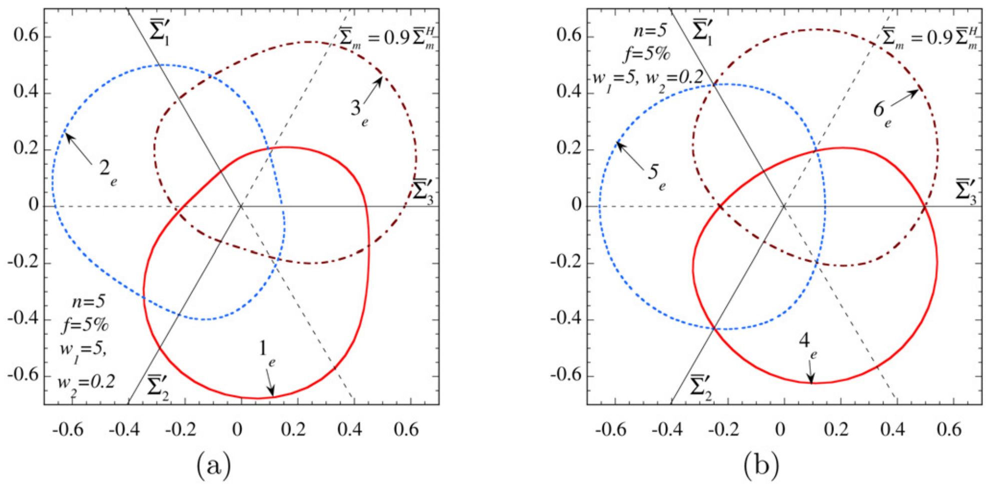

Fig. 6. Cross-sections of the gauge function on the Π-plane (or octahedral plane) for porous media consisting of ellipsoidal voids with aspect ratios $w_1 = 5$ and $w_2 = 0.2$, porosity $f = 5\%$ and nonlinearity $n = 5$. The relevant graphs correspond to the cases that the principal directions of the void are (a) aligned (1_e–3_e) and (b) misaligned (4_e–6_e) with the principal directions of the loading. The cases 1_e–6_e are defined in Table 1.

curve about the origin. Nonetheless, the curves for oblate voids are significantly different in shape than the ones for prolate voids (Fig. 4a).

Fig. 5b shows gauge curves for porous materials consisting of oblate voids whose symmetry axis is misaligned with the principal loading directions. The curves 4_o, 5_o and 6_o correspond to the cases that the symmetry axis of the voids lies in the 2–3, 1–3 and 1–2 plane, as described in Table 1. In this case, the porous medium is still transversely isotropic about a direction that is not parallel to any of the three principal loading directions and, thus, the shape of the gauge curves is very different from those corresponding to the cases 1_o, 2_o and 3_o. Similar to the prolate case, the 4_o, 5_o and 6_o curves are symmetric about the $\overline{\Sigma}'_1$-, $\overline{\Sigma}'_3$- and $\overline{\Sigma}'_2$-axis, respectively, whereas the 5_o and 6_o curves can be obtained by $2\pi/3$ and $4\pi/3$ clockwise rotation of the 1_p curve about the origin. However, this is only due to the specific choice for the orientation of the symmetry axis of the voids relative to the principal loading directions. As already remarked in the context of prolate voids, when the pores are misaligned with the principal loading directions, the corresponding gauge curve is expected to exhibit no symmetry on the Π-plane. This is easily verified by showing in Fig. 5c the case 7_o of oblate voids whose symmetry axis is aligned in the direction [034].

Ellipsoidal voids. Fig. 6 shows *SOM* gauge curves for porous materials consisting of ellipsoidal voids with aspect ratios $w_1 = 5$ and $w_2 = 0.2$. In this case, the behavior of the material is orthotropic in a frame of reference defined by the orientation vectors of the principal axes of the voids, i.e., $\mathbf{n}^{(i)}$ (with $i = 1, 2, 3$). Unlike the previous two configurations involving spheroidal voids, in this case, it is necessary to describe the orientation of all three (or at least two) orientation vectors $\mathbf{n}^{(i)}$ (with $i = 1, 2, 3$) with respect to the unit vectors $\mathbf{e}^{(i)}$ (with $i = 1, 2, 3$). Table 1 includes the six cases 1_e–6_e shown in this figure. More specifically, Fig. 6a presents gauge curves for voids whose principal axes are aligned with the principal loading directions. The main observation in the context of this figure is that the gauge curves 1_e, 2_e and 3_e do not exhibit any symmetry in contrast to the two previous cases involving spheroidal pore shapes. Nevertheless, these curves are all identical in shape, whereas the 2_e and 3_e estimates can be reproduced by $2\pi/3$ and $4\pi/3$ clockwise rotation of the 1_e estimate about the origin.

Fig. 6b shows corresponding curves for ellipsoidal voids whose principal axes are misaligned with the principal loading directions.

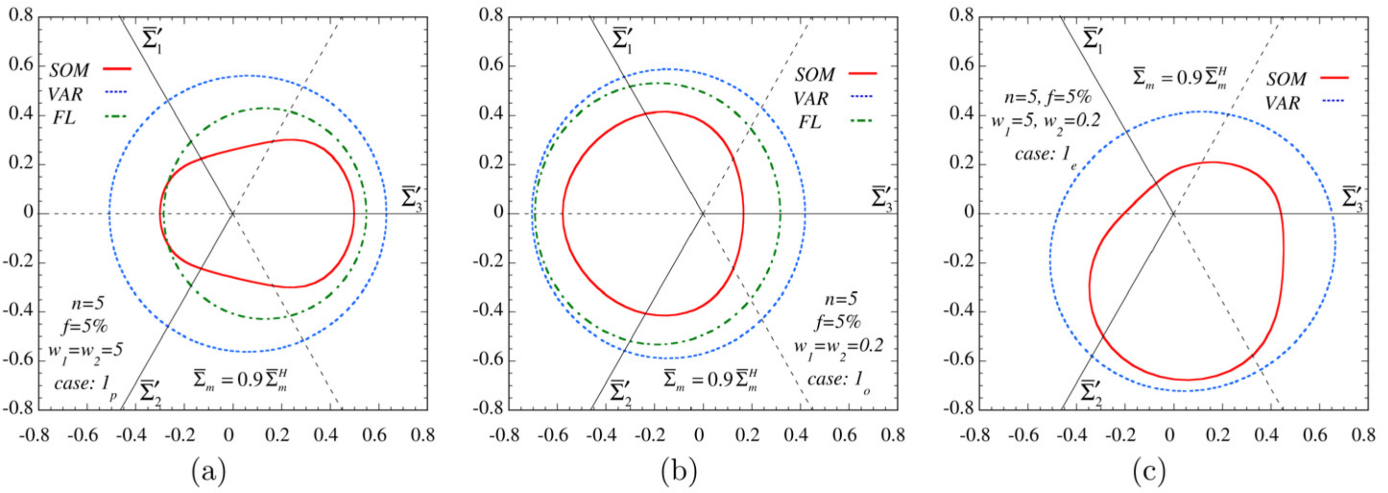

Fig. 7. Comparison of *SOM*, *VAR* and *FL* results for voids with aspect ratios equal to (a) $w_1 = w_2 = 5$ (prolate), (b) $w_1 = w_2 = 0.2$ (oblate) and (c) $w_1 = 5$, $w_2 = 0.2$ (ellipsoids). The cases 1_p, 1_o and 1_e are defined in Table 1.

As a consequence, the shape of the 4_e, 5_e and 6_e curves is substantially different from the ones shown in part (a) of this figure. In the context of Fig. 6b note that the 4_e, 5_e and 6_e curves are symmetric about the $\overline{\Sigma}'_1$-, $\overline{\Sigma}'_3$- and $\overline{\Sigma}'_2$-axis, respectively. This is in contrast with the corresponding curves in part (a) of this figure. This "unexpected" behavior can be explained by noting, for instance, that the 4_e curve corresponds to an ellipsoidal void whose major ($\mathbf{n}^{(2)}$) and minor ($\mathbf{n}^{(3)}$) principal axes were formed by a 45° rotation of the base vectors $\mathbf{e}^{(2)}$ and $\mathbf{e}^{(3)}$, respectively, about the 1-axis leading to a certain symmetry of the material in the 2- and 3-direction. The cases 5_e and 6_e can be explained similar to the case 4_e.

All models. In Fig. 7, we reproduce the *SOM* results for the cases 1_p, 1_o and 1_e, and compare them with *VAR* gauge curves. In addition, we include results obtained by the extended *FL* (Flandi and Leblond, 2005a) model, which is valid only for spheroidal voids.

Fig. 7a shows *SOM*, *VAR* and *FL* gauge curves on the Π-plane for a porous medium consisting of prolate voids with aspect ratios $w_1 = w_2 = 5$, whose symmetry axis is aligned with the $\mathbf{e}^{(3)}$-direction (case 1_p in Table 1). The main observation in the context of this figure is that the *VAR* estimate is significantly stiffer than both the *SOM* and *FL* method. In addition, the *FL* curve seems to have an elliptical shape, similar to the elliptical shape of the *VAR* curve, in contrast with the *SOM* which exhibits a markedly non-elliptical shape being significantly flattened in certain directions. Nonetheless, all estimates are symmetric about the $\overline{\Sigma}'_3$-axis, which is a consequence of the transversely isotropic response of the porous medium under axisymmetric loading along the pore symmetry axis, i.e., $\mathbf{n}^{(3)} = \mathbf{e}^{(3)}$.

Fig. 7b shows corresponding *SOM*, *VAR* and *FL* gauge curves on the Π-plane for a porous medium consisting of oblate voids with aspect ratios $w_1 = w_2 = 0.2$, whose major axis is aligned with the $\mathbf{e}^{(3)}$-direction (case 1_o in Table 1). Here, the *VAR* curve is found to be significantly stiffer than the *SOM* and the *FL* curves, particularly in the positive $\overline{\Sigma}'_3$-axis, while all estimates remain symmetric about this axis due to the transversely isotropic symmetry of the material. In addition, the *FL* curve is very similar with the *VAR* curve, which has an elliptical shape, in contrast with the *SOM* method, which exhibits a flattening across the positive $\overline{\Sigma}'_3$-axis.

Finally, Fig. 7c shows *SOM* and *VAR* gauge curves on the Π-plane for a porous medium consisting of ellipsoidal voids with aspect ratios $w_1 = 5$ and $w_2 = 0.2$, whose principal axes are oriented according to the 1_e case in Table 1. It is emphasized here that the *FL* model cannot handle orthotropic microstructures (i.e., ellipsoidal voids with two different aspect ratios) and thus is not included in this figure. It can be seen that the difference in the shape between the *SOM* and the *VAR* estimates is significant. Due to the orthotropic symmetry of the porous medium, the *SOM* curve exhibits no symmetry, whereas the *VAR* curve remains elliptical, which implies that it has two axes of symmetry. However, those axes of symmetry do not coincide with the axes in the graph.

3. Viscoplasticity: Axisymmetric loading

In this section, we compare the present model (*SOM*) against unit-cell finite element calculations (*FEM*) in order to show explicitly its improvement over the earlier "variational" estimates (*VAR*). For simplicity in the *FEM* calculation, we consider only axisymmetric loading conditions and initially spherical voids.[1]

For this special type of microstructure and loading conditions, it is also meaningful to compare the *SOM* with the most recent Flandi and Leblond (2005b) (*FL*) model, which is valid for axisymmetric loading conditions, provided that during the deformation process the voids remain spheroidal in shape. By contrast, it is emphasized that the *SOM* and *VAR* methods can also handle more general loading conditions (Danas, 2008), such as simple shear loadings presented in Section 4.

3.1. Loading conditions

The *SOM* and the *VAR* refer to random porous media, whereas the *FEM* involves unit-cell calculations with periodic microstructures. Therefore, the comparison between the homogenization methods (*SOM* and *VAR*) and the *FEM* is only meaningful for small concentration of voids (near the dilute limit) (Gilormini and Michel, 1998), where the distribution effects (i.e., random vs. periodic microstructures) are negligible. In this regard, following Koplick and Needleman (1988), Michel et al. (1999), Gărăjeu et al. (2000) and Klöcker and Tvergard (2003), we consider a cylindrical unit-cell consisting of an initially spherical void ($w_1 = w_2 = 1$) with initial porosity $f_o = 0.01\%$. This cell has been introduced as an approximation to a unit-cell of a periodic array of cylindrical cells with hexagonal cross-section.

---

[1] The *FEM* calculations have been performed using the ABAQUS commercial package. A more detailed discussion of the *FEM* computations is provided in Danas (2008).

The unit-cell is subjected to axisymmetric loading conditions such that the only non-zero components of the macroscopic stress tensor $\bar{\boldsymbol{\sigma}}$ are

$$\bar{\boldsymbol{\sigma}} = T\left(\mathbf{e}^{(1)} \otimes \mathbf{e}^{(1)} + \mathbf{e}^{(2)} \otimes \mathbf{e}^{(2)}\right) + S\mathbf{e}^{(3)} \otimes \mathbf{e}^{(3)}, \tag{9}$$

so that S and T serve as the loading parameters in the problem. The stress triaxiality, defined in $(4)_1$, can then be expressed in terms of S and T as

$$X_\Sigma = \frac{S+2T}{3|S-T|} = \frac{S}{|S|}\frac{1+2T/S}{3|1-T/S|}. \tag{10}$$

In the following applications, the stress triaxiality X_Σ (or equivalently the ratio T/S) is kept constant during the deformation process. The values to be used are $X_\Sigma = \pm 1/3, \pm 3$, which correspond to stress ratios $T/S = 0, 0.727$ (with $S \lesseqgtr 0$), respectively. Obviously for the values of T/S given previously, the sign of X_Σ depends on the sign of S. Note that the values $X_\Sigma = \pm 1/3$ correspond to uniaxial tension $(+)$ and compression $(-)$, respectively. On the other hand, the values $X_\Sigma = \pm 3$ represent high triaxiality loadings.

In order to maintain the stress triaxiality constant in the *FEM* calculations, we have used two different methods: we applied (a) constant traction together with periodic boundary conditions and (b) displacement periodic boundary conditions in an implicit form such that the stress triaxiality is kept constant. Both approaches predicted the same results for the cases discussed below. On the other hand, numerical problems started occurring at high nonlinearities, i.e., for $n > 10$. For this reason, we do not include results for the ideally-plastic case where the *FEM* calculations are mesh-dependent, particularly when strain hardening is not included and the material is prone to strong localization.

As a consequence of the axisymmetric loading, the initially spherical voids evolve into spheroidal ones with prolate or oblate shape, whereas their principal axes remain fixed during the deformation process (leading to transversely isotropic symmetry for the material). This implies that the two aspect ratios are equal, i.e., $w_1 = w_2 = w$ and the principal axes of the voids coincide with the principal loading directions, i.e., $\mathbf{n}^{(i)} = \mathbf{e}^{(i)}$ $(i = 1, 2, 3)$. For convenience with the notation, henceforth, we will make use of the aspect ratio w to denote the change in the shape of the spheroidal voids. The cases $w = 1$, $w > 1$ and $w < 1$ correspond to spherical, prolate and oblate voids, respectively. At this point, it should be noted that in the *FEM* calculations the void does not preserve an ellipsoidal shape during the deformation process, especially at high nonlinearities and large deformations. Therefore, the "principal axes" of the void can only be defined in approximate terms. In the present work, w is computed by the ratio of the lateral and horizontal axes of the void (see Danas (2008) for more details). This procedure has been found to be sufficiently accurate for most of the loadings considered in the following except in some degenerate cases where special reference will be made.

Due to the alignment of the loading (9) with the pore symmetry axis, the resulting macroscopic strain-rate $\overline{\boldsymbol{D}}$ is also axisymmetric, i.e., $\bar{D}_{11} = \bar{D}_{22} \neq 0$, $\bar{D}_{33} \neq 0$ and $\bar{D}_{ij} = 0$ for $i \neq j$. Using this fact, it is useful to introduce the axial and equivalent macroscopic strain measures, $\bar{\varepsilon}_{33}$ and $\bar{\varepsilon}_{eq}$, respectively, given by

$$\bar{\varepsilon}_{33} = \int_0^t \bar{D}_{33}\,\mathrm{d}t, \qquad \bar{\varepsilon}_{eq} = \frac{2}{3}\int_0^t |\bar{D}_{33} - \bar{D}_{11}|\,\mathrm{d}t, \tag{11}$$

which serve as time-like variables. For later use, it is also pertinent to define the equivalent strain-rate $\dot{\varepsilon}_{eq}^{\infty}$ in the absence of voids, which reads

$$\dot{\varepsilon}_{eq}^{\infty} = \dot{\varepsilon}_o \left(\frac{\bar{\sigma}_{eq}}{\sigma_o}\right)^n. \tag{12}$$

In this expression, σ_o is the flow stress of the matrix phase and $\dot{\varepsilon}_o$ is a reference strain-rate taken in the following calculations equal to unity.

Finally, several nonlinear exponents are used, i.e., $n = 1, 2, 4, 10$. It should be recalled that the values $n = 1$ and $n = 10$ correspond to a linear and strongly nonlinear viscoplastic material, respectively. The effect of the stress triaxiality X_Σ and the nonlinearity n on the evolution of the microstructural and macroscopic variables is studied in detail in the following subsections.

3.2. Tensile loadings: comparison among several models

Uniaxial tension loading with $X_\Sigma = 1/3$ (or $T/S = 0$ with $S > 0$). In Fig. 8, we consider a uniaxial tension loading, where the relevant evolution variables are shown as a function of the axial strain $\bar{\varepsilon}_{33}$ for a nonlinearity $n = 10$. The main feature of this loading predicted by all estimates shown in Fig. 8a is that the porosity f/f_o grows initially but it approaches an asymptote for sufficiently large strains (Ponte Castañeda and Zaidman, 1994; Benzerga, 2002; Lassance et al., 2007). Here, the *SOM* is in much better agreement with the *FEM* predictions than the *FL* and the *VAR* models. On the other hand, in Fig. 8b, the *SOM* overestimates the evolution of the aspect ratio w, while the *FL* method is in very good agreement with the *FEM* results. The *VAR* method underestimates the evolution of w, as already anticipated. Looking at Fig. 8c, the *SOM*

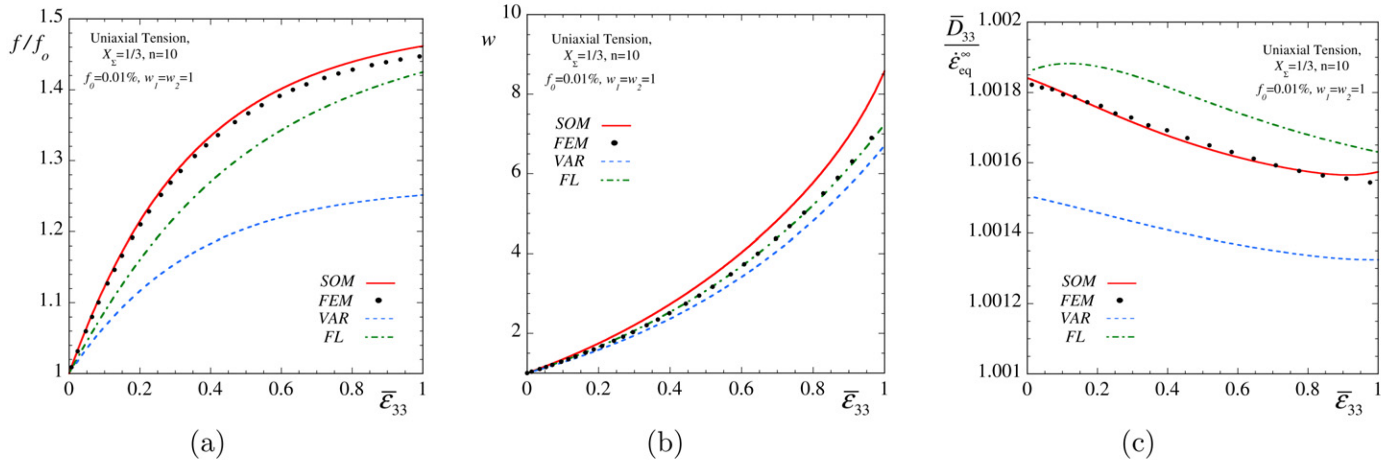

(a) (b) (c)

Fig. 8. *SOM*, *FEM*, *FL* and *VAR* curves for the evolution of (a) the normalized porosity f/f_o $(f_o = 0.01\%)$, (b) aspect ratio w and (c) the normalized axial strain-rate $\bar{D}_{33}/\dot{\varepsilon}_{eq}^{\infty}$ ($\dot{\varepsilon}_{eq}^{\infty}$ is the corresponding strain-rate in the absence of voids) for a nonlinear exponent $n = 10$ under uniaxial tension loading ($X_\Sigma = 1/3$ and $T/S = 0$ with $S > 0$).

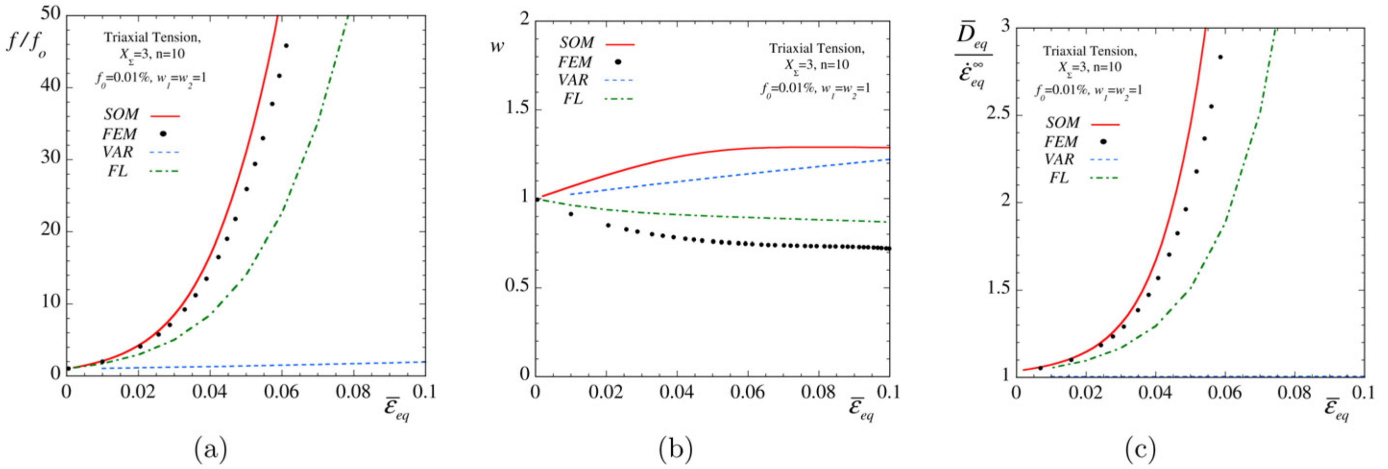

(a) (b) (c)

Fig. 9. *SOM*, *FEM*, *FL* and *VAR* curves for the evolution of (a) the normalized porosity f/f_o ($f_o = 0.01\%$), (b) aspect ratio w and (c) the normalized equivalent strain-rate $\overline{D}_{eq}/\dot{\varepsilon}^\infty_{eq}$ ($\dot{\varepsilon}^\infty_{eq}$ is the corresponding strain-rate in the absence of voids) for nonlinear exponents $n = 10$ under triaxial tension loading ($X_\Sigma = 3$ and $T/S = 0.727$ with $S > 0$).

estimates for the normalized axial strain-rate $\overline{D}_{33}/\dot{\varepsilon}^\infty_{eq}$ improve significantly on the *VAR* results, being in very good agreement with the *FEM* predictions. In contrast, the *FL* method exhibits a somewhat different qualitative behavior from the *FEM* and the *SOM* results.

Triaxial tension loading with $X_\Sigma = 3$ **(or** $T/S = 0.727$ **with** $S > 0$**).** In Fig. 9 the relevant evolution variables are shown as a function of the macroscopic equivalent strain $\bar{\varepsilon}_{eq}$ for a nonlinearity $n = 10$. In part (a) of this figure, both the *SOM* and *FEM*, which are found to be in very good agreement, predict a very rapid increase of the normalized porosity f/f_o. In contrast, the *FL* estimate, although showing a rapid increase of f/f_o, it tends to underestimate the evolution of the porosity. Note that the corresponding *VAR* estimate for f/f_o is way off. In turn, in Fig. 9b, the aspect ratio w evolves insignificantly, taking values close to unity, i.e., the voids remain roughly spherical in shape for this high triaxiality loading. However, it is interesting to note that at this high nonlinearity ($n = 10$) the void elongates in the direction transverse to the maximum principal stress (see that $w < 1$), as predicted by the *FEM* results. In other words, the initially spherical void evolves into an oblate void. This interesting effect has initially been observed by Budiansky et al. (1982) and Fleck and Hutchinson (1986) in the dilute case. Such an effect is a direct consequence of the nonlinearity of the matrix phase and the high triaxiality loading, which induce a certain distribution of strains around the void resulting in this unexpected phenomenon. This effect is captured qualitatively by the *FL* model, whereas the *SOM* and *VAR* estimates predict that the void becomes slightly prolate ($w > 1$) in shape.

Even though the *SOM* does not predict accurately the evolution of w, it remains in good agreement with the *FEM* results, certainly better than the *FL* estimates, for the evolution of the equivalent macroscopic strain-rate $\overline{D}_{eq}/\dot{\varepsilon}^\infty_{eq}$. In contrast, the *VAR* method severely underestimates the evolution of the porosity f/f_o and as a consequence fails to capture accurately the evolution of the normalized macroscopic strain-rate $\overline{D}_{eq}/\dot{\varepsilon}^\infty_{eq}$ and therefore the effective response of the porous medium. In this regard, the main conclusion in the context of this high triaxiality loading is that the evolution of the porosity f/f_o is predominant over the evolution of the aspect ratio w, hence controlling the overall behavior of the composite. The improvement of the *SOM* over the *VAR* estimates for this high triaxiality loading is attributed to the fact that the *SOM* is constructed such that it recovers the analytical CSA (composite sphere assemblage) result in purely hydrostatic loading, in contrast with the *VAR* method, which is too stiff in this case (see Section 3.4 in Part I of this work).

3.3. Compressive loadings: comparison among several models

Uniaxial compression loading with $X_\Sigma = -1/3$ **(or** $T/S = 0$ **with** $S < 0$**).** In Fig. 10, we consider uniaxial compression loading conditions with a nonlinear exponent $n = 10$. Part (a), provides comparisons of the various models for the evolution of the normalized porosity f/f_o as a function of the absolute macroscopic axial strain $|\bar{\varepsilon}_{33}|$. The main observation in the context of this figure is that, while the *SOM*, the *FL* and the *FEM* predictions are in good agreement during the whole deformation process (up to the closure of the porosity), the *VAR* method overestimates significantly the evolution of f/f_o almost by $\sim 40\%$. On the contrary, in Fig. 10b, all the methods exhibit the same qualitative behavior for the evolution of the aspect ratio w. Nonetheless, they progressively deviate from each other, with the *VAR* estimate delivering the highest values for w. It should be mentioned, here, that because of the strong nonlinearity of the matrix phase the void shape in the *FEM* calculation deviates significantly from being a spheroid developing contact zones at low values of f/f_o. This suggests that special numerical care needs to be taken in order to ensure material impenetrability. Furthermore, the ratio between the "geometrical" major and minor axes of the void does not constitute an appropriate measure of the aspect ratio w in this degenerate case (see details on Section 3.5 in Danas (2008)). Since the main objective of this work is to provide a qualitative and, if possible, a quantitative comparison to the *SOM* estimates, for simplicity, the *FEM* calculations are terminated when the void develops these contact zones.

Fig. 10c shows corresponding plots for the normalized macroscopic axial strain-rate $|\overline{D}_{33}|/\dot{\varepsilon}^\infty_{eq}$. In this figure, the *SOM* and the *FEM* predictions are in very good agreement, whereas the corresponding *FL* results are found to be qualitatively different from the previous two methods. The *VAR* method, in turn, underestimates the evolution of $|\overline{D}_{33}|/\dot{\varepsilon}^\infty_{eq}$ as a consequence of the poor estimation for the evolution of the porosity. It is worth noting that both the *SOM* and the *VAR* estimates exhibit sharp increases in the estimate for $|\overline{D}_{33}|/\dot{\varepsilon}^\infty_{eq}$, in contrast with the *FL* model which shows a sharp decrease. In the first two cases of the *SOM* and *VAR* estimates, this sharp increase is linked to the rapid decrease of the aspect ratio w, which is found to reduce faster than the normalized porosity f/f_o leading to the formation of cracks. The converse is true for the *FL* model, whereas no definitive conclusions can be drawn for the corresponding *FEM* curve due to the cut off point.

Triaxial compression loading with $X_\Sigma = -3$ **(or** $T/S = 0.727$ **with** $S < 0$**).** Fig. 11 shows evolution plots for a stress triaxial-

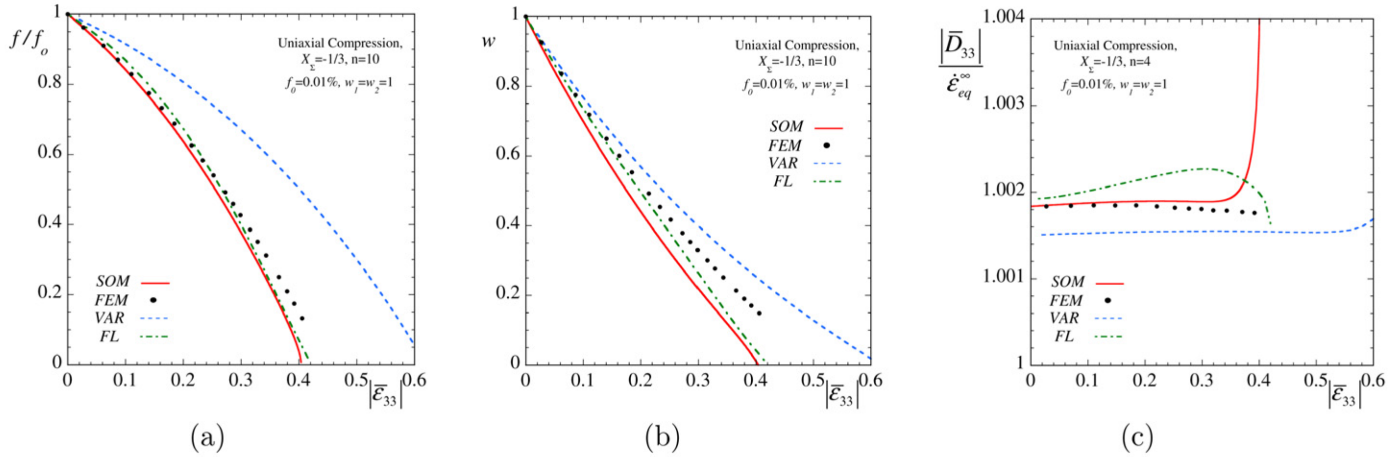

Fig. 10. *SOM*, *FEM*, *FL* and *VAR* curves for the evolution of (a) the normalized porosity f/f_o ($f_o = 0.01\%$), (b) aspect ratio w and (c) the normalized axial strain-rate $|\bar{D}_{33}|/\dot{\varepsilon}^{\infty}_{eq}$ ($\dot{\varepsilon}^{\infty}_{eq}$ is the corresponding strain-rate in the absence of voids) for nonlinear exponents $n = 10$ under uniaxial compression loading ($X_\Sigma = -1/3$ and $T/S = 0$ with $S < 0$).

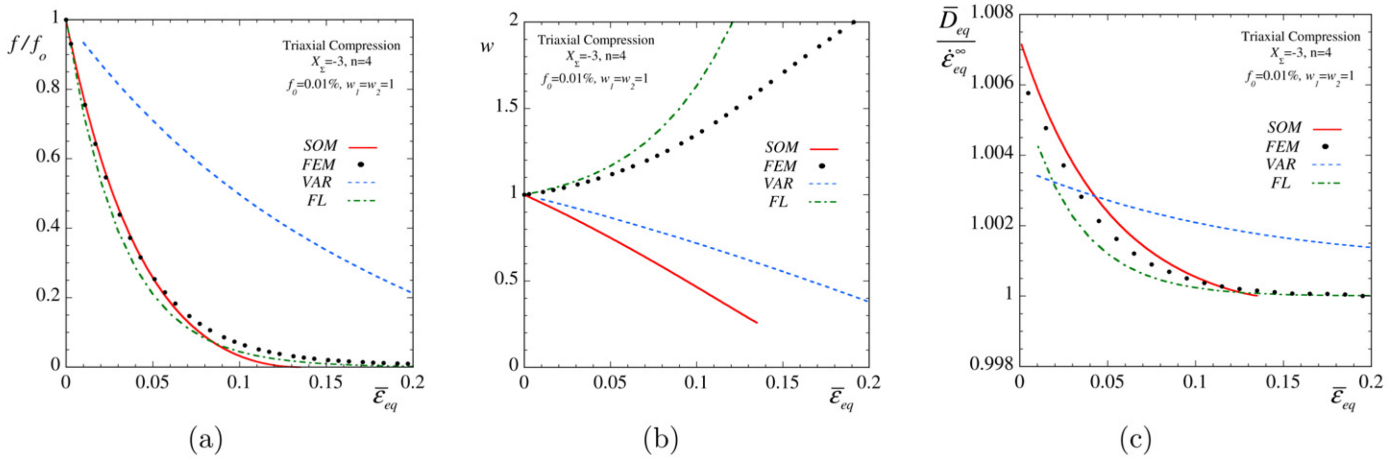

Fig. 11. *SOM*, *FEM*, *FL* and *VAR* curves for the evolution of (a) the normalized porosity f/f_o ($f_o = 0.01\%$), (b) aspect ratio w and (c) the normalized equivalent strain-rate $\bar{D}_{eq}/\dot{\varepsilon}^{\infty}_{eq}$ ($\dot{\varepsilon}^{\infty}_{eq}$ is the corresponding strain-rate in the absence of voids) for nonlinear exponents $n = 4$ under uniaxial compression loading ($X_\Sigma = -3$ and $T/S = 0.727$ with $S < 0$).

ity $X_\Sigma = -3$ as a function of the equivalent macroscopic strain $\bar{\varepsilon}_{eq}$ for a nonlinear exponent $n = 4$. Fig. 11a shows the evolution of the normalized porosity f/f_o, where all (but the *VAR*) methods are in very good agreement. As already anticipated, for high triaxialities the *VAR* method overestimates the evolution of the porosity due to the overly stiff predictions for hydrostatic loadings. In Fig. 11b, in turn, the various models deliver very different estimates for the evolution of the aspect ratio w, with the *FL* model being in qualitative agreement with the *FEM* results. This disagreement between the various methods is due to the fact that the void elongates in a direction parallel to the maximum compressive principal stress taking a prolate shape ($w > 1$). This is a "local" phenomenon that occurs at sufficiently high triaxialities and nonlinearities as already discussed in the context of Fig. 9b. However, it is interesting to note that even though the *SOM* provides a poor estimate for the aspect ratio w, it predicts with remarkable accuracy the normalized macroscopic equivalent strain-rate $\bar{D}_{eq}/\dot{\varepsilon}^{\infty}_{eq}$ when compared with the corresponding *FEM* and *FL* results. This apparent paradox can be easily explained by the fact that for high-triaxiality loadings the evolution of porosity f/f_o is so dramatic that it completely controls the effective behavior of the porous material, whereas the corresponding evolution of the aspect ratio w is significant only at a local level and thus does not affect the overall behavior of the composite. Of course, the *VAR* estimate provides poor estimates for the evolution of the porosity and consequently fails to give accurate estimates for the evolution of $\bar{D}_{eq}/\dot{\varepsilon}^{\infty}_{eq}$.

3.4. Effect of the nonlinearity

The objective of this brief subsection is to discuss the effect of the nonlinearity on the evolution of the relevant microstructural variables. In this connection, Fig. 12 shows corresponding results for uniaxial tension loading with $X_\Sigma = 1/3$ (or $T/S = 0$ with $S > 0$) as a function of the nonlinear exponent ($n = 1, 2, 4, 10$) and the macroscopic axial strain $\bar{\varepsilon}_{33}$. In Fig. 12a, the predictions of the *SOM* for the evolution of the normalized porosity f/f_o are in very good agreement with the *FEM* results for all the nonlinearities considered. In Fig. 12b, the *SOM* tends to overestimate slightly the evolution of the aspect ratio w, when compared with the corresponding *FEM* predictions. It is remarked, however, that for this loading the evolution of the aspect ratio does not depend strongly on the nonlinearity of the matrix phase, certainly much less than the corresponding evolution of the porosity. On the other hand, the corresponding *VAR* evolution curves for f/f_o and w do not depend on the nonlinearity and they all coincide with the $n = 1$ curve. In this regard, the *SOM* is found to improve significantly on the earlier *VAR* method, especially at high nonlinearities. Finally, Fig. 12c shows the evolution of the normalized macroscopic axial strain-rate $\bar{D}_{33}/\dot{\varepsilon}^{\infty}_{eq}$. The agreement between the *SOM* and the

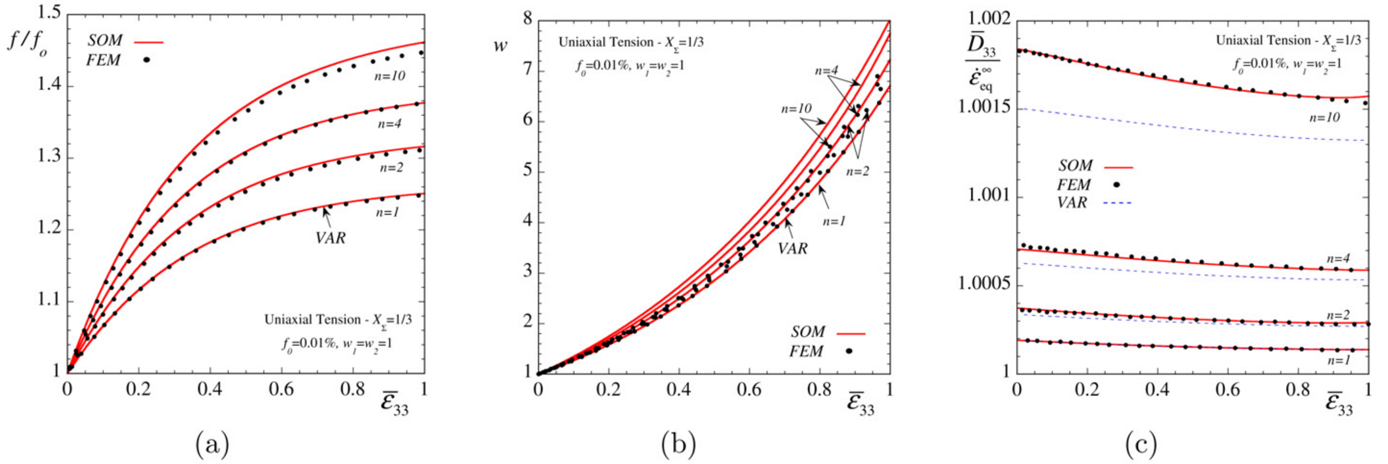

Fig. 12. *SOM*, *VAR* and *FEM* curves for the evolution of (a) the normalized porosity f/f_o ($f_o = 0.01\%$), (b) aspect ratio w and (c) the normalized axial strain-rate $\overline{D}_{33}/\dot{\varepsilon}^{\infty}_{eq}$ ($\dot{\varepsilon}^{\infty}_{eq}$ is the corresponding strain-rate in the absence of voids) for nonlinear exponents $n = 1, 2, 4, 10$ under uniaxial tension loading ($X_{\Sigma} = 1/3$ and $T/S = 0$ with $S > 0$).

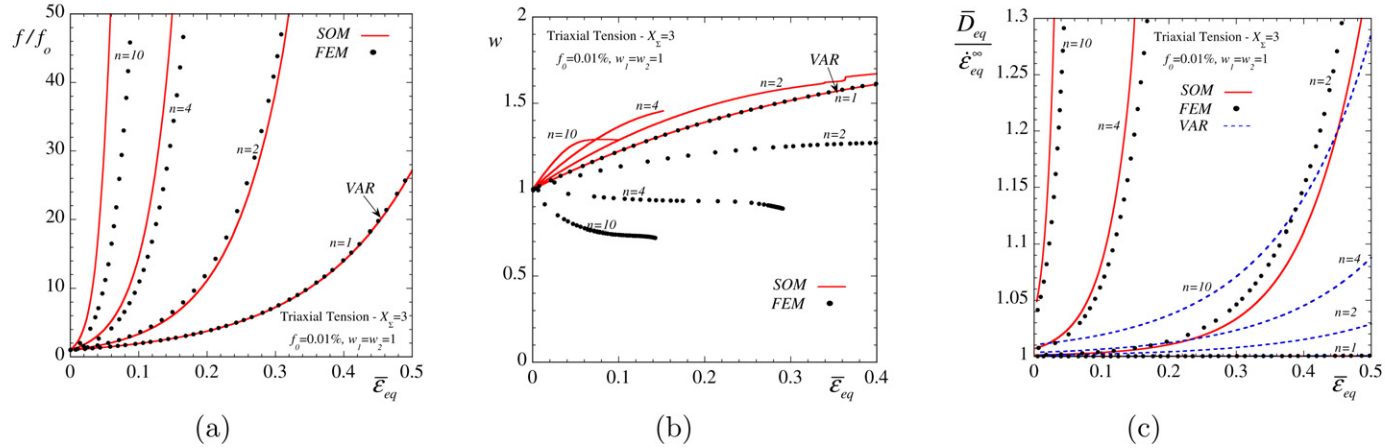

Fig. 13. *SOM*, *VAR* and *FEM* curves for the evolution of (a) the normalized porosity f/f_o ($f_o = 0.01\%$), (b) aspect ratio w and (c) the normalized equivalent strain-rate $\overline{D}_{eq}/\dot{\varepsilon}^{\infty}_{eq}$ ($\dot{\varepsilon}^{\infty}_{eq}$ is the corresponding strain-rate in the absence of voids) for nonlinear exponents $n = 1, 2, 4, 10$ under triaxial tension loading ($X_{\Sigma} = 3$ and $T/S = 0.727$ with $S > 0$).

FEM estimates is remarkable even at very high nonlinearities (i.e., $n = 10$). In contrast, the corresponding *VAR* model underestimates the evolution of $\overline{D}_{33}/\dot{\varepsilon}^{\infty}_{eq}$, particularly at high nonlinearities.

Fig. 13 shows corresponding evolution plots for triaxial tension loading with $X_{\Sigma} = 3$ or $T/S = 0.727$ with $S > 0$ as a function of the nonlinear exponent $n = 1, 2, 4, 10$ and the macroscopic equivalent strain $\bar{\varepsilon}_{eq}$. At this high triaxiality loading, the effect of the nonlinearity on the evolution of f/f_o is rather dramatic, as shown in Fig. 13a. The *SOM* and the *FEM* are in very good agreement in this case, while the *SOM* improves significantly on the earlier *VAR* method, which is independent of the nonlinearity n and thus, all the *VAR* estimates coincide with the $n = 1$ curve.

In Fig. 13b, the aspect ratio of the void w evolves only slightly, while remaining very close to its initially spherical shape. Note that for $n > 4$ the void evolves into an oblate shape as previously discussed in the context of Fig. 9b. However, even though the *SOM* method is not able to capture this very nonlinear "local" effect accurately, it remains in remarkable agreement with the *FEM* predictions for the normalized macroscopic strain-rate $\overline{D}_{eq}/\dot{\varepsilon}^{\infty}_{eq}$, as can be observed in Fig. 13c. This is a direct consequence of the fact that the *SOM* is able to predict accurately the evolution of porosity f/f_o, which clearly dominates over the evolution of the aspect ratio w in this case of high triaxiality. In contrast, the *VAR* underestimates significantly the evolution of the porosity and hence the evolution of $\overline{D}_{eq}/\dot{\varepsilon}^{\infty}_{eq}$.

4. Viscoplasticity: Simple shear loading

In this section, we consider a porous material with initially spherical voids and porosity $f_o = 1\%$ under simple shear loading. More specifically, we apply a velocity gradient with the only nonzero component being $\overline{L}_{23}$, such that $\overline{D}_{23} = \overline{\Omega}_{23}$. The total amount of shear is then defined as

$$\bar{\gamma} = \int_{0}^{t} \overline{L}_{23}\,\mathrm{d}t \tag{13}$$

serving as a time-like variable. The rest of the components of the average strain-rate $\overline{\boldsymbol{D}}$ and average spin $\overline{\boldsymbol{\Omega}}$ are zero. While the porosity does not evolve during the deformation process (since $\overline{D}_{ii} = 0$), the shape of the voids is expected to change. In addition, due to the applied macroscopic spin $\overline{\Omega}_{23}$, the principal axes of the voids lying on the plane 2–3 are also expected to evolve in time. For this reason, it is convenient to introduce the Euler angle ψ, such that

$$\mathbf{n}^{(1)} = \mathbf{e}^{(1)}, \qquad \mathbf{n}^{(2)} = \cos\psi\,\mathbf{e}^{(1)} + \sin\psi\,\mathbf{e}^{(2)},$$
$$\mathbf{n}^{(3)} = -\sin\psi\,\mathbf{e}^{(1)} + \cos\psi\,\mathbf{e}^{(2)}. \tag{14}$$

For a better understanding of the following results, we note that the unit vectors $\mathbf{n}^{(2)}$ and $\mathbf{n}^{(3)}$ correspond to the longer and shorter principal axis respectively of the ellipsoidal voids (i.e.,

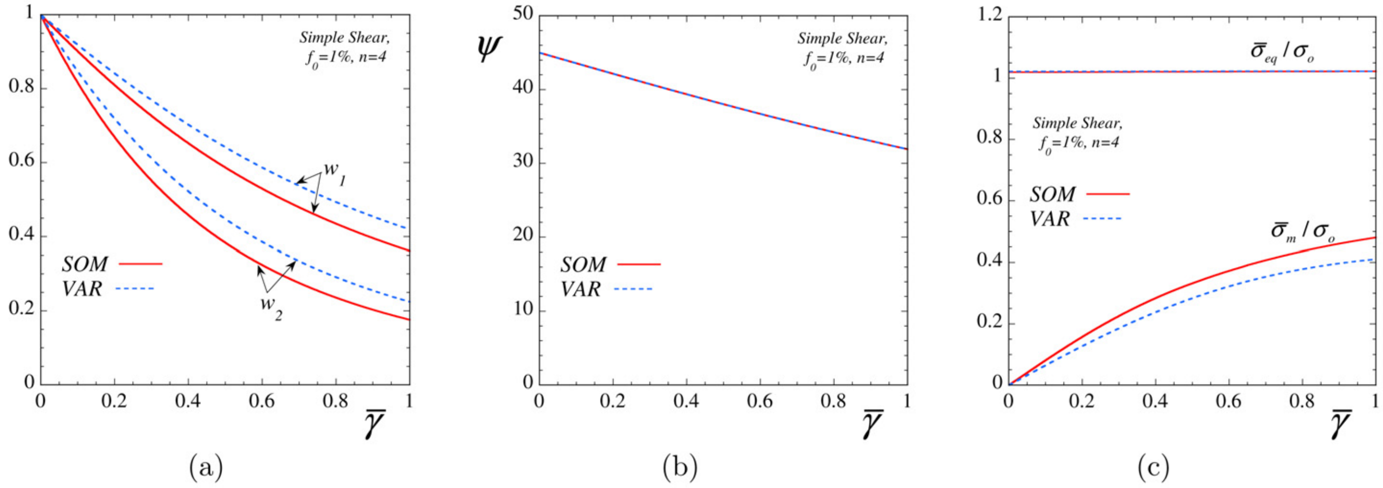

(a) (b) (c)

Fig. 14. *SOM* and *VAR* curves for the evolution of (a) the two aspect ratios w_1 and w_2, (b) the orientation angle ψ of the voids in the plane of shear for prescribed $\bar{D}_{23} = \bar{\Omega}_{23}$ and (c) the equivalent and mean macroscopic normalized stress $\bar{\sigma}_{eq}/\sigma_o$ and $\bar{\sigma}_m/\sigma_o$. The nonlinearity is $n = 4$ and the initial porosity $f_o = 1\%$. The porosity does not change during the process and hence is not shown here.

$w_2 \leqslant w_1 \leqslant 1$). Therefore, the angle ψ in (14) defines the direction of the longer principal axis of the voids on the plane of deformation relative to the $\mathbf{e}^{(2)}$ axis.

Fig. 14 shows the evolution of the aspect ratios w_1 and w_2, the orientation angle ψ and the equivalent and mean macroscopic normalized stress $\bar{\sigma}_{eq}/\sigma_o$ and $\bar{\sigma}_m/\sigma_o$ as a function of the amount of shear $\bar{\gamma}$ for both the *SOM* and the *VAR* methods. The nonlinearity of the matrix phase is $n = 4$. In part (a) of this figure, both models generate voids with ellipsoidal shapes (i.e., $w_1 \neq w_2$), whereas the *SOM* predicts a sharper decrease of the two aspect ratios w_1 and w_2 than the *VAR* method which is known to be identical with the $n = 1$ (linear) case, as already discussed in the previous subsection. On the other hand, in part (b), the voids are elongated initially at 45°, i.e., in the direction of maximum stretching, and rotate clockwise as $\bar{\gamma}$ increases. Here, the *SOM* and *VAR* estimates for the orientation angle ψ coincide, which indicates that the evolution of ψ does not depend on the nonlinearity of the matrix phase in this case. In turn, in part (c) of this figure, the *SOM* and *VAR* estimates for $\bar{\sigma}_{eq}/\sigma_o$ are in very close agreement, whereas for the hydrostatic part of $\bar{\boldsymbol{\sigma}}$, the *SOM* predicts a higher $\bar{\sigma}_m/\sigma_o$ than the *VAR*. It is noted here that the normal components $\bar{\sigma}_{11}$, $\bar{\sigma}_{22}$ and $\bar{\sigma}_{33}$ become non-zero and evolve as the deformation progresses (because of the developing anisotropy in the material). This in turn suggests that the shearing direction is not parallel to the evolving principal axes of the voids as the deformation progresses. Unfortunately, we were not able to provide comparisons with *FEM* results in this fully three-dimensional case, but comparisons with *FEM* results have been carried out (Danas et al., 2008c) for transverse shear of a porous material with cylindrical voids. This comparisons demonstrate the satisfactory performance of the model at least in that case.

Finally, it is noted that the Gurson-type models, such as the model of Flandi and Leblond (2005a, 2005b) cannot be used for this special, albeit important, case of simple shear loading, since they cannot handle general ellipsoidal shapes ($w_1 \neq w_2 \neq 1$), as well as changes in the orientation of the principal axes of the voids, and could not therefore be included in Fig. 14. In fact, the original Gurson (1977) model, which incorporates no information about the void shape, predicts a constant equivalent stress $\bar{\sigma}_{eq}/\sigma_o = \sqrt{1 + f_o^2}$ and a zero hydrostatic stress $\bar{\sigma}_m/\sigma_o = 0$ for the entire deformation process. As a consequence, the material does not exhibit any softening or hardening at finite deformations leading to unrealistic estimates (Aravas and Ponte Castañeda, 2004; Nahshon and Hutchinson, 2008; Tvergaard, 2008).

5. Ideal-plasticity: Plane-strain loading and instabilities

In this section, following earlier work by Ponte Castañeda and Zaidman (1994) and Kailasam and Ponte Castañeda (1998), we make use of the new "second-order" (*SOM*) model and the earlier "variational" (*VAR*) method to study the effective response and possible development of shear localization in porous materials with an ideally-plastic matrix phase subjected to plane-strain loading conditions with fixed stress triaxiality X_Σ.

We consider a porous medium with initial porosity $f_o = 1\%$ subjected to plane-strain loading ($\bar{D}_{22} = 0$), such that the stress triaxiality remains constant during the deformation process. This can be accomplished by setting $\bar{D}_{33}$ equal to $+1$ (or -1), and solving for $\bar{D}_{11}$ to enforce the condition

$$X_\Sigma = c, \tag{15}$$

where c is a positive (or negative) constant. In addition, $\bar{D}_{ij} = 0$ for $i \neq j$, which implies that we induce no change in the orientation of the principal axes of the voids. Note further that the macroscopic equivalent strain (given in (11) for axisymmetric loading conditions) is redefined here (for consistency with standard usage in the literature) as

$$\bar{\varepsilon}_{eq} = \int_0^t \bar{D}_{eq}\,\mathrm{d}t = \frac{2}{3}\int_0^t \sqrt{\bar{D}_{33}^2 - \bar{D}_{11}\bar{D}_{33} + \bar{D}_{11}^2}\,\mathrm{d}t, \tag{16}$$

and therefore serves as a time-like variable in the problem. It should be emphasized that, for the above-described loading, $\bar{\varepsilon}_{eq} \neq \sqrt{2\bar{\varepsilon}_{ij}\bar{\varepsilon}_{ij}/3}$, with $\bar{\varepsilon}_{ij} = \int_0^t \bar{D}_{ij}\,\mathrm{d}t$.

In connection with the previous relations, the computation of the effective Jaumann hardening rate H_J simplifies considerably, since in this case the Jaumann rates and the standard time derivatives of the relevant quantities coincide. Thus, it follows from the analysis made in Section 5.3 of Part I that the Jaumann hardening rate reduces to

$$H_J = H = -\left\{ y_f \frac{\partial \widetilde{\Phi}}{\partial f} + \sum_{i=1}^{2} y_w^{(i)} \frac{\partial \widetilde{\Phi}}{\partial w_i} \right\}, \tag{17}$$

for the loading conditions (15). In this expression, $\widetilde{\Phi} = 0$ is the effective yield condition (see Section 5.1 of Part I of this work), while the functions y_f and $y_w^{(i)}$ have been defined in Section 5.3 of Part I.

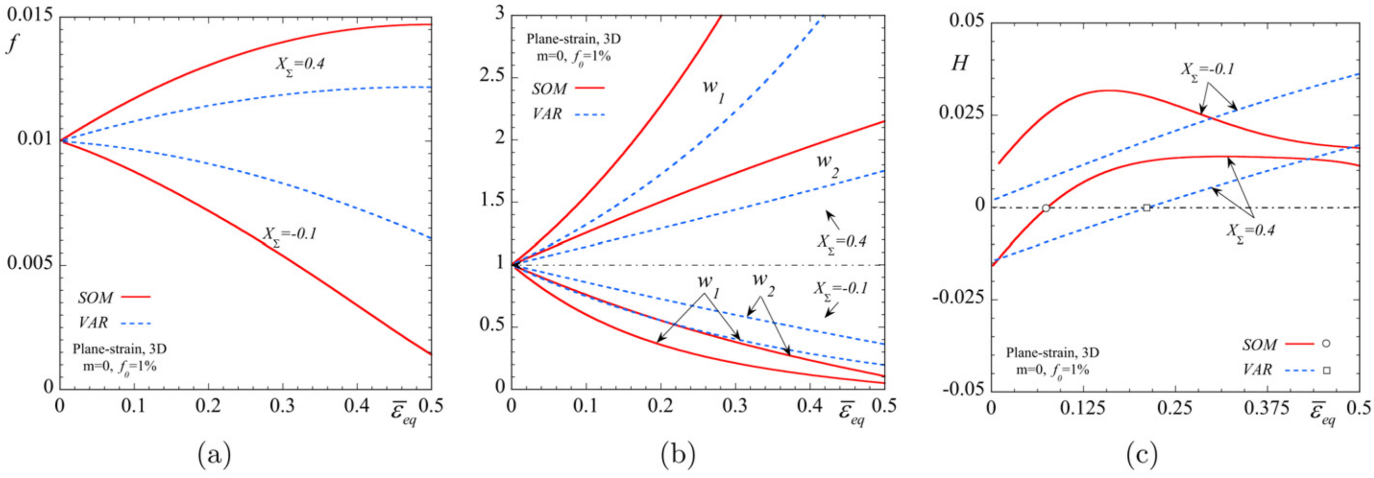

Fig. 15. *SOM* and *VAR* estimates are shown for $X_\Sigma = -0.1, 0.4$ and initially spherical pores. The evolution curves correspond to (a) the porosity f, (b) the aspect ratio w, and (c) the hardening rate of the composite as a function of the macroscopic, equivalent strain $\bar{\varepsilon}_{eq}$. In (c) the symbols $\circ$ and $\square$ denote the loss of ellipticity for the porous medium as predicted by the *SOM* and the *VAR*, respectively.

Sufficient conditions for shear localization in rigid-plastic materials have been provided by Rice (1976). The first condition is related to the determination of the critical hardening rate H_{cr}, which, for the previously described loading, can be shown to reduce to $H_{cr} = 0$. The second condition, which states that there should exist a non-deforming surface in the deformation field, is satisfied easily due to the plane-strain character of the problem provided that the in-plane strain-rate components be of opposite signs, i.e., $\overline{D}_{11}\overline{D}_{33}$ be negative. Therefore, in the following results, a vanishing hardening rate ($H = 0$) together with $\overline{D}_{11}\overline{D}_{33} < 0$ implies shear localization for the porous medium.

Fig. 15 shows evolution curves for the porosity f (Fig. 15a), the aspect ratios w_1 and w_2 (Fig. 15b), and the hardening rate H (Fig. 15c) as a function of the macroscopic equivalent strain $\bar{\varepsilon}_{eq}$ for a porous medium with initially spherical voids ($w_1 = w_2 = 1$). The representative values $X_\Sigma = -0.1$ and $X_\Sigma = 0.4$ are considered.

In Fig. 15a, the corresponding *SOM* estimate for $X_\Sigma = 0.4$ predicts an initially high positive rate of growth of the porosity f, whereas at a finite strain (e.g., $\bar{\varepsilon}_{eq} \sim 50\%$), f attains a maximum. The same observation is also true for the *VAR* estimate with the only difference that the growth of f is weaker than in the *SOM* case. Note that the increase of the porosity is a softening mechanism. On the other hand, in Fig. 15b, the fast rate of change in the aspect ratios results in the hardening of the material in the direction of maximum stretching (i.e., in the 3-direction). This is true for both the *SOM* and the *VAR* methods, while for the *SOM* the rate of increase of w_1 and w_2 is higher than for the *VAR* method. As a result of these two competing mechanisms, the porous material exhibits initial softening, which evolves into overall hardening at larger strains, as shown in Fig. 15c, where both the *SOM* and the *VAR* curves for H cross zero at some (different) finite strains. The critical strain $\bar{\varepsilon}^{cr}_{eq}$ at which H becomes zero, as predicted by the *SOM* and the *VAR* models, respectively, is denoted by the symbols $\circ$ and $\square$ in Fig. 15c. As already mentioned earlier, when $H = 0$ the porous material may become unstable, provided that the product $\overline{D}_{11}\overline{D}_{33}$ is negative (which is true in this case, although not shown explicitly in the figures). Clearly, both the *SOM* and the *VAR* methods predict such a macroscopic shear localization instability. However, the critical strain, where the instability occurs, is different with the *SOM* being lower than the *VAR*.

On the other hand, for $X_\Sigma = -0.1$, the *SOM* predicts a faster decrease of the porosity than the *VAR* method, and thus a faster hardening of the porous medium, as shown in Fig. 15a. In Fig. 15b, the corresponding *SOM* and *VAR* estimates for the evolution of the aspect ratios w_1 and w_2, both of which decrease with the deformation, indicate that the material softens faster in the direction of the maximum principal strain. When these two contradicting mechanisms, i.e., the evolution of porosity and the aspect ratios, are combined together, they result in overall hardening of the porous medium, which is illustrated by the initial positive hardening rate H in Fig. 15c, for both methods. This geometrical hardening of the porous medium continues as the deformation progresses, and as a consequence, the material does not exhibit instabilities, which is deduced by observing that H never attains the zero value.

Furthermore, it should be emphasized that in the Gurson (1977) model (not included here for clarity of the results in Fig. 15), the porosity f is the only hardening/softening mechanism. More specifically, for tensile loadings (e.g., $X_\Sigma > 0$), the porosity increases leading to the softening of the porous medium (i.e., $H < 0$), while for compressive ones (e.g., $X_\Sigma < 0$), the porosity decreases leading to the overall hardening of the porous material (i.e., $H > 0$) for the entire deformation process. For $X_\Sigma = 0$, the Gurson model predicts no change in the porosity and hence $H = 0$ as the deformation progresses. This is the only case that the Gurson model satisfies, albeit trivially, the Rice conditions for a shear localization instability. By comparison of the Gurson model with the results presented in Fig. 15 for the *SOM* and the *VAR* models, we deduce that the changes in the void shape (i.e., in the aspect ratios w_1 and w_2) provide the key physical mechanism for making the hardening rate H cross the zero axis (by inducing an additional geometrical softening/hardening in the deformation of the porous material).

The procedure of identifying an instability point, described previously, can be repeated for the entire range of stress triaxialities $X_\Sigma \in (-\infty, +\infty)$. Accordingly, Fig. 16 presents a map of the critical strain $\bar{\varepsilon}^{cr}_{eq}$, where the instability occurs, as a function of the prescribed stress triaxiality X_Σ, for two initial porosities (a) $f_o = 1\%$ and (b) $f_o = 10\%$. It is interesting to note that the *SOM* and the *VAR* predictions are qualitatively similar (although quite different in quantitative terms) for $f_o = 1\%$, and very similar for $f_o = 10\%$. Thus, for both initial porosities considered here, the *SOM* and *VAR* methods predict no instabilities for stress triaxialities higher than $X_\Sigma \gtrsim 0.6$, as well as for negative ones ($X_\Sigma < 0$). In turn, it should be pointed out that the Gurson model only predicts (trivially) an instability for $X_\Sigma = 0$ and for this reason it has not been included in Fig. 16.

At this point, it should be emphasized that the present analysis is strictly valid for plane-strain loading conditions and porous ma-

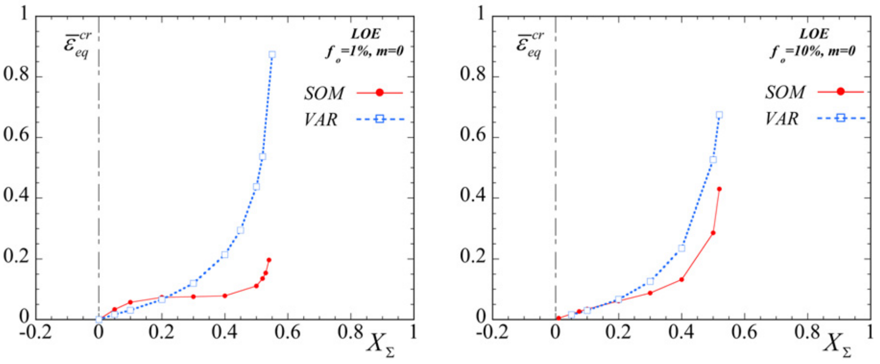

(a) (b)

Fig. 16. Macroscopic onset-of-failure maps as predicted by the *SOM* and *VAR* methods, for an initially isotropic porous medium with ideally-plastic matrix phase and initial porosity (a) $f_o = 1\%$ and (b) $f_o = 10\%$. The plot shows the critical equivalent strain $\bar{\varepsilon}_{eq}^{cr}$ as a function of the applied stress triaxiality X_Σ.

terials with an ideally-plastic matrix phase. Predictions for more realistic situations will require taking into account elastic and hardening effects in the matrix phase. Such extensions are relatively straightforward to incorporate, and will be used in future work to make comparisons with experimental results for other loading conditions, including plane stress and axisymmetric loading states (Bao and Wierzbicki, 2004; Barsoum and Faleskog, 2007).

6. Concluding remarks

In this work, we have obtained homogenization estimates for random porous media with viscoplastic (including ideally-plastic) matrix phases and ellipsoidal voids subjected to general loading conditions. These estimates were derived by making use of the framework developed in Part I of this work, which is based on the nonlinear "second-order" homogenization method of Ponte Castañeda (2002a). The major result of this work is the dramatic improvement of the new model on the earlier "variational" estimates of Ponte Castañeda (1991), Ponte Castañeda and Zaidman (1994), Kailasam and Ponte Castañeda (1998), Aravas and Ponte Castañeda (2004) for high-triaxiality loading conditions. This improvement is a direct consequence of the fact that the new model is constructed in such a way that it recovers exactly the behavior of a "composite-sphere assemblage" in the limit of hydrostatic loadings. On the other hand, the new model preserves all the features already present in the initial formulation of the "variational" (Ponte Castañeda, 1991) and "second-order" (Ponte Castañeda, 2002b) homogenization methods, and thus is capable of providing estimates for general loading conditions and ellipsoidal microstructures.

The "second-order" model has been compared with the recent Flandi and Leblond (2005a, 2005b) model for the prediction of the instantaneous behavior of transversely isotropic porous materials consisting of aligned spheroidal voids subjected to axisymmetric loading conditions aligned with the pore symmetry axis. The agreement between the two models was better for prolate than for oblate voids. However, the new model allows for the consideration of more general (non-spheroidal) ellipsoidal microstructures leading to significantly different effective behaviors, as intuitively expected. In addition, it has been observed that, for all microstructural configurations considered in this study, involving prolate, oblate and ellipsoidal voids, the relative orientation of the voids with respect to the principal loading directions can have dramatic effects on the instantaneous effective response of the porous medium.

Furthermore, the predictions of the new "second-order" model for finite-strain loading histories has been validated by comparison with unit-cell finite element calculations and corresponding results obtained by the earlier "variational" method and the Flandi and Leblond (2005a, 2005b) model. The "second-order" model has been found to improve significantly on the earlier "variational" method, which was shown to provide estimates that are independent of the nonlinearity of the matrix phase, while remaining overly stiff at high stress triaxialities. We have also shown that both the "second-order" and the Flandi–Leblond models provide accurate estimates for the determination of the effective response of the porous medium for axisymmetric loading conditions and initially spherical voids. In particular, the present model delivers better results for the evolution of the porosity and the macroscopic strain-rate, for the stress triaxialities considered here. On the other hand, the Flandi–Leblond model can capture nonlinear effects regarding the evolution of the aspect ratio of the voids at high triaxialities. Such effects were first discussed by Budiansky et al. (1982) and Fleck and Hutchinson (1986), who found that at sufficiently high triaxialities and nonlinearities the voids elongate in a direction that is transverse to the maximum principal strain or stress. However, we found that this counter-intuitive elongation of the void at high triaxialities does not appear to have a significant effect on the macroscopic response of the porous composite, which is mainly controlled by the evolution of the porosity at high stress triaxialities (and is captured quite accurately by the "second-order" model).

In addition to the aforementioned *aligned* loadings, we have also considered a simple shear (i.e., non-aligned) loading. In this case, both the "second-order" and "variational" models predict a change in the orientation of the voids, which take on ellipsoidal shapes (i.e., two different aspect ratios) during the deformation process. As a consequence of the induced anisotropy in the material, normal components of the macroscopic stress develop as the deformation progresses. In this connection it should be emphasized that no other model in the literature can capture these features associated with this basic loading history.

Finally, following prior work by Ponte Castañeda and Zaidman (1994) and Kailasam and Ponte Castañeda (1998), the "second-order" and the "variational" methods have been applied to porous media with an ideally-plastic matrix phase subjected to plane-strain loading conditions with fixed stress triaxiality loading. An important conclusion resulting from the study of this problem is that the various microstructural variables interact in complex ways such that the final response of the material may exhibit overall geometric softening or hardening. This geometric softening or hardening of the porous medium can lead to macroscopic shear localization instabilities (Rice, 1976). In this regard, the present model (and the earlier "variational" method) provides a concrete theoretical framework for the prediction of macroscopic shear localization instabilities and is expected to be complementary to earlier models, such as the one by Gurson (1977) and its recent extensions by Nahshon and Hutchinson (2008), Leblond and Mottet (2008) and Xue (2008), which assume that the microstructure remains isotropic during the deformation history, and are therefore not capable of accurately capturing the induced geometrical softening (or hardening) of the material for low-triaxiality loading conditions. In this connection, it should be mentioned that recent work by Michel et al. (2007) has demonstrated the physical relevance of these "macroscopic" instabilities in the related context of porous elastomers. Finally, numerical implementation of the present model in a general purpose finite element subroutine would allow consideration of engineering applications, as well as the comparison of the new estimates proposed in this work with experimental results by Bao and Wierzbicki (2004) and Barsoum and Faleskog (2007), particularly for shear loading conditions. Such work is now underway and will be reported elsewhere.

Acknowledgements

The authors would like to thank Professor Nikolaos Aravas for his valuable comments and advice, especially with the *FEM* simulations. The work of K.D. was supported in part by the international fellowship "Gaspard Monge" at the École Polytechnique and partially by the scholarship for Hellenes of the Alexander S. Onassis Public Benefit Foundation. The work of K.D. and P.P.C. was also supported by the US National Science Foundation through Grants CMS-02-01454 and OISE-02-31867.

References

Aravas, N., Ponte Castañeda, P., 2004. Numerical methods for porous metals with deformation-induced anisotropy. Comput. Methods Appl. Mech. Engrg. 193, 3767–3805.

Bao, Y., Wierzbicki, T., 2004. On the fracture locus in the equivalent strain and stress triaxiality space. Int. J. Mech. Sci. 44, 1768–1786.

Barsoum, I., Faleskog, J., 2007. Rupture mechanisms in combined tension and shear–Experiments. Int. J. Solids Struct. 44, 1768–1786.

Benzerga, A.A., 2002. Micromechanics of coalescence in ductile fracture. J. Mech. Phys. Solids 50, 1331–1362.

Budiansky, B., Hutchinson, J.W., Slutsky, S., 1982. Void growth and collapse in viscous solids. In: Hopkins, H.G., Sewell, M.J. (Eds.), Mechanics of Solids, The Rodney Hill 60th Anniversary Volume. Pergamon Press Oxford, pp. 13–45.

Danas, K., 2008. Homogenization-based constitutive models for viscoplastic porous media with evolving microstructure. Ph.D. thesis, LMS, École Polytechnique, http://www.polymedia.polytechnique.fr/Center.cfm?Table=These.

Danas, K., Idiart, M.I., Ponte Castañeda, P., 2008a. A homogenization-based constitutive model for two-dimensional viscoplastic porous media. C. R. Mecanique 336, 79–90.

Danas, K., Idiart, M.I., Ponte Castañeda, P., 2008b. A homogenization-based constitutive model for isotropic viscoplastic porous media. Int. J. Solids Struct. 45, 3392–3409.

Danas, K., Idiart, M.I., Ponte Castañeda, P., 2008c. A homogenization-based constitutive model for two-dimensional viscoplastic porous media with evolving microstructure. In: Jeulin, D., Forest, S. (Eds.), Continuum Models and Discrete Systems (CMDS 11). Mines-Paris Tech, Paris, pp. 143–148.

Danas, K., Ponte Castañeda, P., 2009. A finite-strain model for viscoplastic anisotropic porous media: I – Theory. Eur. J. Mech. A/Solids 28 (3), 387–401.

Flandi, L., Leblond, J.-B., 2005a. A new model for porous nonlinear viscous solids incorporating void shape effects – I: Theory. Eur. J. Mech. A/Solids 24, 537–551.

Flandi, L., Leblond, J.-B., 2005b. A new model for porous nonlinear viscous solids incorporating void shape effects – II: Numerical validation. Eur. J. Mech. A/Solids 24, 552–571.

Fleck, N.A., Hutchinson, J.W., 1986. Void growth in shear. Proc. R. Soc. Lond. A 407, 435–458.

Gărăjeu, M., Michel, J.-C., Suquet, P., 2000. A micromechanical approach of damage in viscoplastic materials by evolution in size, shape and distribution of voids. Comput. Methods Appl. Mech. Engrg. 183, 223–246.

Gilormini, P., Michel, J.-C., 1998. Finite element solution of the problem of a spherical inhomogeneity in an infinite power-law viscous matrix. Eur. J. Mech. A/Solids 17, 725–740.

Gurson, A.L., 1977. Continuum theory of ductile rupture by void nucleation and growth. J. Engng. Mater. Technol. 99, 2–15.

Kachanov, L.M., 1971. Foundations of the Theory of Plasticity. North-Holland, Amsterdam.

Kailasam, M., Ponte Castañeda, P., 1998. A general constitutive theory for linear and nonlinear particulate media with microstructure evolution. J. Mech. Phys. Solids 46, 427–465.

Klöcker, H., Tveergard, V., 2003. Growth and coalescence of non-spherical voids in metals deformed at elevated temperature. Int. J. Mech. Sciences 45, 1283–1308.

Koplick, J., Needleman, A., 1988. Void growth and coalescence in porous plastic solids. Int. J. Solids Struct. 24, 835–853.

Lassance, D., Fabrègue, D., Delannay, F., Pardoen, T., 2007. Micromechanics of room and high temperature fracture in 6xxx Al alloys. Progress in Materials Science 52, 62–129.

Leblond, J.-B., Mottet, G., 2008. A theoretical approach of strain localization within thin planar bands in porous ductile materials. C. R. Mecanique 336, 176–189.

Lee, B., Mear, M., 1992. Axisymmetric deformation of power-law solids containing a dilute concentration of aligned spheroidal voids. J. Mech. Phys. Solids 40, 1805–1836.

Lubliner, J., 1990. Plasticity Theory. Macmillan Publishing Company.

Michel, J.-C., Moulinec, H., Suquet, P., 1999. Effective properties of composite material with periodic microstructure: A computational approach. Comput. Methods Appl. Mech. Engrg. 172, 109–143.

Michel, J.-C., Lopez-Pamies, O., Ponte Castañeda, P., Triantafyllidis, N., 2007. Microscopic and macroscopic instabilities in finitely strained porous elastomers. J. Mech. Phys. Solids 55, 900–938.

Nahshon, K., Hutchinson, J.W., 2008. Modification of the Gurson model for shear failure. Eur. J. Mechanics A/Solids 27, 1–17.

Ponte Castañeda, P., 1991. The effective mechanical properties of nonlinear isotropic composites. J. Mech. Phys. Solids 39, 45–71.

Ponte Castañeda, P., 2002a. Second-order homogenization estimates for nonlinear composites incorporating field fluctuations. I. Theory. J. Mech. Phys. Solids 50, 737–757.

Ponte Castañeda, P., 2002b. Second-order homogenization estimates for nonlinear composites incorporating field fluctuations. II. Applications. J. Mech. Phys. Solids 50, 759–782.

Ponte Castañeda, P., Zaidman, M., 1994. Constitutive models for porous materials with evolving microstructure. J. Mech. Phys. Solids 42, 1459–1497.

Rice, J.R., 1976. The localization of plastic deformation. In: Koiter, W.T. (Ed.), Proceedings of the 14th International Congress of Theoretical and Applied Mechanics. North-Holland Publishing Company, pp. 207–220.

Tvergaard, V., 2008. Shear deformation of voids with contact modelled by internal pressure. Int. J. Mech. Sciences 50, 1459–1465.

Xue, L., 2008. Constitutive modeling of void shearing effect in ductile fracture of porous materials. Engng. Fract. Mech. 75, 3343–3366.